Development of control-oriented models for a building under regular heating, ventilation and air-conditioning operation – a comparative simulation study and an experimental validation

Heman Shamachurn* and Sayed Z. Sayed Hassen

Department of Electrical and Electronic Engineering,
University of Mauritius,
Reduit 80837, Mauritius
Email: h.shamachurn@uom.ac.mu
Email: z.sayedhassen@uom.ac.mu
*Corresponding author

Abstract: The development of models is a major barrier to the fast and widespread adoption of model predictive control for building HVAC systems. This paper proposes the subspace identification technique, refined through the prediction error method, to quickly obtain a model for the accurate indoor temperature prediction, even with little identification data, even in the presence of large unmeasured disturbances and noisy identification data, and even using data which was collected during the regular HVAC operation of a building. The identification issues associated with grey-box models were thoroughly investigated. In particular, the development of a grey-box model was found to be a complex, lengthy and computationally intensive process, even for a single-zone building, and the models were not physically meaningful. The proposed method was found to be much easier and faster, with a potential for direct practical application. Analysis on experimental data from an existing building provided promising results.

Keywords: subspace identification; regular HVAC operation; open-loop data; closed-loop data; RC model; experimental validation; DesignBuilder.

Reference to this paper should be made as follows: Shamachurn, H. and Hassen, S.Z.S. (2023) 'Development of control-oriented models for a building under regular heating, ventilation and air-conditioning operation – a comparative simulation study and an experimental validation', *Int. J. Modelling, Identification and Control*, Vol. 42, No. 1, pp.83–104.

Biographical notes: Heman Shamachurn received his Bachelor's in Electrical and Electronic Engineering from the University of Mauritius, Mauritius, and Master of Science in Renewable Energy Systems Technology from Loughborough University, UK. He has worked in industry for nearly two years, and is currently a Senior Lecturer at the University of Mauritius. He has research interests in renewable energy systems, and building energy modelling and control.

Sayed Z. Sayed Hassen graduated with a BEng (hons.) in Electrical Engineering, MEngSc in Electrical Engineering from the Monash University, Australia and then went on to pursue his PhD in Electrical Engineering at University of New South Wales, Australia. He has also worked as an Electronic Hardware Design Engineer in Australia for over two years and has over 20 years experience in academia. His research interest is in control systems engineering. He is currently an Associate Professor at the University of Mauritius.

1 Introduction

Buildings consume about 30% of the global energy use (IEA, 2019), with heating, ventilation and air-conditioning (HVAC) systems consuming about 37% of that (Ürge-Vorsatz et al., 2015). The improvement of existing building energy management systems through advanced control technologies is a promising avenue to improve the energy efficiency of buildings (Salakij et al., 2016). Inappropriate sensing and controls, and the inability to explore the full potential of existing building control systems are responsible for about 30% of energy-wasting in commercial buildings (Kim and Katipamula, 2018). The traditional ON/OFF and proportional-integral-derivative (PID) controllers are widely used in many HVAC systems due to their ease of design and implementation. However, they are not as energy-efficient as predictive control methods such as model predictive control (MPC) (Dadiala et al., 2020; Schubnel et al., 2020). MPC has numerous advantages including the ability to perform anticipatory control rather than corrective control, to include a disturbance model for disturbance rejection, to handle constraints and uncertainties, and to deal with time-varying system dynamics as well as various operating conditions

(Afram and Janabi-Sharifi, 2014). MPC has shown its capability to regulate the internal environmental conditions of a space more efficiently than conventional control techniques (Hu et al., 2019; Ryzhov et al., 2019). MPC was also shown to outperform optimised PID control on plants varying from first to fifth order (Salem et al., 2015).

MPC requires a model which can reproduce the thermal dynamics of the building with an acceptable level of accuracy and with minimal complexity. The model development stage is still the most time consuming, tedious, and expensive part of an MPC implementation project (Martincevic and Vasak, 2019). Building thermal models can be classified into white, black and grey-box categories. White-box models, being highly complex, require expert knowledge for their development, and are nearly impossible to be tuned to experimental data. Black-box models are the quickest to develop, but they convey very little physical information such that they cannot be generalised. Moreover, they require a large amount of training data and have a performance depending on the data quality (Delcroix et al., 2020). Grey-box models are developed using physical principles and are calibrated using measurement data. The resistance-capacitance (RC) grey-box models (Li et al., 2010; Kim et al., 2020) have been the focus of most works on MPC as applied to buildings. A brief summary of recent works on the development of linear time invariant (LTI) building thermal models is provided next.

Delcroix et al. (2020) studied the indoor temperature simulation results of RC and black-box autoregressive model with exogenous inputs (ARX) models. The RC parameters were identified through optimisation. The resulting model had a poor performance as it was under-parameterised, while the ARX model could not capture the nonlinear thermal processes. Cui et al. (2019) used RC models to predict the average building indoor temperature. The model parameters were identified through particle swarm optimisation which minimised the root mean square error (RMSE) between the simulated and measured temperatures. The solar gain was calculated using the direct normal irradiance, which is not usually measured on a site. The sol-air temperature was used to obtain the heat transfer through opaque fabrics. The determination of this temperature involves uncertainties given that some parameters have to be assumed. The developed models achieved mean absolute errors (MAEs) and RMSEs in the ranges of 0.48–0.63°C and 0.61–0.78°C, respectively. Wang et al. (2019b) developed RC and ARX models for a single zone building. EnergyPlus was used to create persistently exciting identification data. The RC parameters were identified through a gradient-free optimisation technique (Wang et al., 2019a), whereby the MAE between the actual and the modelled air temperatures was minimised. Blum et al. (2019) investigated the impacts of different modelling aspects on the final operating costs. The sum of squared error (SSE) between the emulator model zone temperature and the developed model's temperature was minimised. A third order RC (3R3C) model for a single zone was found to provide the best balance between accuracy and complexity. The physical meaningfulness of the identified parameters was not studied in detail. Moreover, the impacts of unknown disturbances and initial states were not addressed in the work. Wang and Chen (2019) reviewed data-driven model development techniques. RC and ARX models were also developed for a house. The RC model had the worst fit. It was claimed that a better fit could possibly be obtained with a more complex structure, but the parameter estimates could be physically meaningless. Brastein et al. (2018) investigated the dispersion of estimated RC parameters. The parameters were identified through constrained optimisation. The resulting zone temperature simulation error was below 2°C for a seven-day period, and this figure was claimed to be usable in an MPC framework. The identified parameters, however, could not be assigned a physical meaning related to the building properties. Viot et al. (2018a) performed an extensive analysis to identify suitable RC models from experimental identification data. The best model resulted in an MAE of only 0.78°C and was used in a MPC framework for a real building (Viot et al., 2018b). Prívara et al. (2013) proposed the subspace identification approach whereby a third order model per zone was used. An EnergyPlus model of a multi-zone building was used to generate persistently exciting identification data. The only performance evaluation metric was the normalised RMSE, and occupancy heat gains were assumed to be known perfectly. Noisy identification data was not considered. The 12-hours ahead normalised RMSE varied in the range of 35%–80% for the different thermal zones. The temperature predictions involved large absolute errors of up to 3°C for the eight-hours ahead prediction. Similarly, Cigler and Prívara (2010) employed the subspace identification to obtain a usable model for MPC, without performing detailed analyses.

1.1 Research justification

The development of control-oriented thermal models is still the most complicated, time-consuming and expensive part of a model-based control project (Martincevic and Vasak, 2019). Most existing publications have simply emphasised the satisfactory development of a thermal model which suited their application, but their proposed approaches may not be applicable for other works, because of lack of generality. Moreover, the aim of most publications was to lay emphasis on the potential economic benefits of MPC, without stressing on the details about the model development itself. Thus, this work compares the development of LTI control-oriented thermal models using the following three techniques: optimisation, prediction-error-minimisation (PEM) and subspace identification. The issues associated with the first two methods were identified through detailed analyses. Grey-box models have been widely used, but there is a lack of results to emphasise the impacts of the following factors: suitable objective function, unknown initial states, unknown disturbances, size of the parameter search space, noisy identification data, and local optima resulting from optimisation. Moreover, the subspace identification method

has remained underexploited for applications in HVAC control. In addition, no work has used the data collected during the regular HVAC operation to compare different model estimation techniques. Furthermore, most works have considered the generation of suitable identification data through system excitation, rather than trying to develop models using normal HVAC operational data, which would be a cheaper alternative than running expensive experiments. It should be noted that forcing experiments on HVAC systems may also not be always possible, considering the associated time and safety issues (Atam and Helsen, 2016). Eventually, no work has employed subspace identification to perform extensive analyses using data collected during the normal HVAC operation of either an emulator model or a real building, but this has been studied in this work.

1.2 Contribution and practical usefulness of this work

The significant contributions of this work are as follows.

Firstly, the impacts of the following factors on the identification of RC grey-box models were studied using open-loop data: unknown initial state, unknown disturbances, selection of the objective function, size of the parameter search space, noise in the identification data, and processing of results involving local optima. These factors have not been explicitly studied by other works reported in literature.

Secondly, nonlinear constrained optimisation, PEM, and subspace identification methods were used to produce a suitable control-oriented model using closed-loop identification data. The latter was obtained by simulating an office building under regular (unforced) HVAC operation, while most works in literature have dealt with identification data produced through system excitation (Cigler and Prívara, 2010; Prívara et al., 2013; Atam and Helsen, 2016; Joe and Karava, 2017). The issues associated with the different identification techniques were analysed and compared. The literature contains no work dealing with a thorough comparison of the subspace identification method to other techniques, and this was achieved in this work. In addition, the developed subspace model was refined through PEM in order to enhance the quality of the prediction model, and such an approach was not found in literature.

Thirdly, experimental data was collected from a real building whose HVAC system was under regular operation. The data was used to identify a control-oriented model using the subspace identification technique. The initial model was subsequently refined through PEM. The quality and the performance of the models were thoroughly investigated. Particularly, the prediction accuracies over different horizons, the different performance evaluation metrics, the autocorrelation and cross-correlation of residuals, and the non-availability of particular inputs were investigated in order to confirm the promising outcomes of the technique. To the best of the authors' knowledge, such a detailed analysis using subspace identification applied to experimental data is not available in literature. Moreover, given that occupancy-based heat gains are difficult to be quantified, they will not act as good inputs to the black-box thermal models. Hence, the use of CO_2 concentration measurements as a substitute was investigated in this work.

The results of this work will be useful to guide model developers in areas where an acceptable thermal model for MPC is needed over a reasonable time frame. Section 2 discusses the methodology employed and Section 3 presents the simulation results. We conclude the findings and provide avenues for further work in Section 4.

2 Methodology

2.1 Model to generate open-loop data

One way to determine the effectiveness of any given plant identification technique is to test it on a known plant. A second order RC model shown in Figure 1 was selected to represent the plant. T_o was the outside air temperature in °C, T_z was the measured zone air temperature in °C and T_{im} was the internal mass temperature in °C. Q_{sol} was the global horizontal irradiance (GHI) in kW/m^2. Factor A in m^2 decided about the part of Q_{sol} through the glazings which was absorbed by the indoor air, while factor B in m^2 determined the part of Q_{sol} which was absorbed by the internal mass of the zone (Tang and Wang, 2019; Wang et al., 2019a, 2019b). Q_{hvac} was the heating/cooling power in kW and was assumed to be convective only, and Q_{dist} was the total disturbance heat gains from occupants in kW, equipment and lighting. R_e was the thermal resistance linking the outdoor air to the zone air in K/kW, and R_{im} was the thermal resistance linking the zone air to the internal mass of the zone in K/kW. C_{im} was the thermal capacitance of the internal thermal mass in kJ/K and C_z was the zone air thermal capacitance in kJ/K. The values of the chosen model parameters are provided in Table 1. These values were chosen somewhat arbitrarily, given that it was the back-identification results which were important, and not the chosen parameter values.

Figure 1 Second order RC model

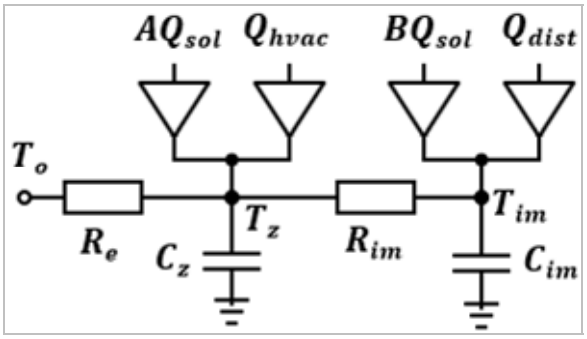

The continuous-time dynamic state-space model is described by equations (1) and (2).

$$C_z\dot{T}_z = \frac{T_o - T_z}{R_e} + \frac{T_{im} - T_z}{R_{im}} + AQ_{sol} + Q_{hvac} \quad (1)$$

$$C_{im}\dot{T}_{im} = \frac{T_z - T_{im}}{R_{im}} + BQ_{sol} + Q_{dist} \quad (2)$$

where $[T_z, T_{im}]$ is the state vector. To enable the use of sampled input-output data, the continuous-time model was discretised with a sampling time period of five minutes using the zero-order hold technique and the resulting discrete time state-space model is shown in equations (3) and (4).

$$\begin{bmatrix} T_z(k+1) \\ T_{im}(k+1) \end{bmatrix} = [A_d] \begin{bmatrix} T_z(k) \\ T_{im}(k) \end{bmatrix} + [B_d] \begin{bmatrix} T_o(k) \\ Q_{sol}(k) \\ Q_{hvac}(k) \\ Q_{dist}(k) \end{bmatrix} \quad (3)$$

$$[y(k)] = [C_d] \begin{bmatrix} T_z(k) \\ T_{im}(k) \end{bmatrix} \quad (4)$$

where A_d, B_d and C_d are the discrete-time state-space model matrices.

Figure 2 Input-output data

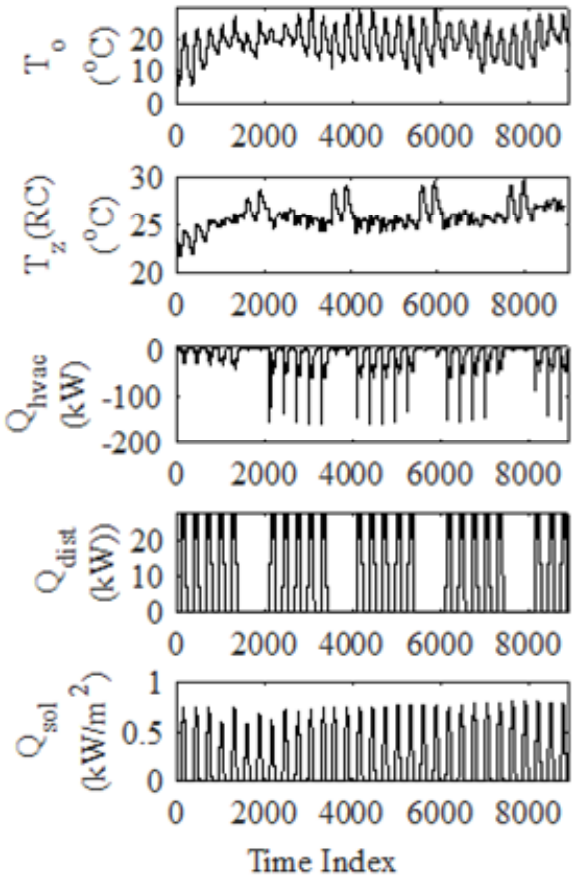

The discrete time model was then simulated with the input data shown in Figure 2 and a chosen initial state of $[T_z, T_{im}]$ = [23.5, 25]. The resulting model output representing the zone air temperature (T_z) is also shown in Figure 2. This temperature was then used along with the known inputs Q_{sol}, T_o, Q_{hvac} and Q_{dist} to back identify the model as described in Section 2.3.

Table 1 Second order model parameters

Parameter	*Value*	*Units*
A	36.08	m^2
B	56.31	m^2
R_e	0.429	K/kW
R_{im}	0.128	K/kW
C_{im}	8.39×10^5	kJ/K
C_z	1.34×10^5	kJ/K

2.2 *Emulator model of a building to generate closed-loop identification data*

The considered building is shown in Figure 3 and was assumed to be used for an open office, with a floor area of 625 m^2, a roof area of 625 m^2, a wall area of 190 m^2, a window area of 160 m^2 and a zone volume of 1,975 m^3. While many works have reported having low glazing fractions facing a specific direction, this work has considered a building with significant glazing in all the four facades.

Figure 3 Single zone building simulated in DesignBuilder (see online version for colours)

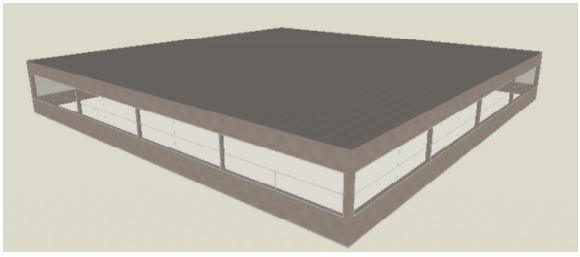

The walls were made of lightweight concrete block rendered on both the interior and exterior sides. The resistance and capacitance of the walls were 6.60 K/kW and 14,820 kJ/K, respectively. The roof comprised an exterior bitumen water-proofing layer on the reinforced concrete layer which was rendered on the interior. The resistance of the roof was 0.446 K/kW and its capacitance was 144,375 kJ/K. The floor was assumed to be an intermediate floor of a building. It was made of reinforced concrete, rendered on the exterior of the thermal zone, and tiled on the interior. An adiabatic block was placed below the floor to avoid heat transfer between the considered thermal zone and the below storey of the building. The inner surface resistance of the floor was 0.272 K/kW. The floor capacitance was 130,625 kJ/K. The glazing had a resistance of 1.08 K/kW. The capacitance of the zone air was 1,832 kJ/K.

The heating and cooling set points were 21°C and 25°C, respectively. The heating and cooling set back temperatures were 16°C and 30°C, respectively. The HVAC system was a fan coil unit (four-pipe) with an air cooled chiller. The occupancy schedule was set as for a typical office operating during weekdays only with an occupancy density of 0.1 people/m^2. The power density for computer heat gain was set at 10 W/m^2. The zone capacitance multiplier was set

as 10 to cater for the contents of the zone such as furniture and equipment. Model infiltration and window shading were not considered in this work. The lighting normalised power density was set as 5 W/m^2, with a radiant fraction of 0.1, visible fraction of 0.18 and convective fraction of 0.72. The lighting and equipment heat output patterns were in line with the occupancy schedule.

Figure 4 DesignBuilder results – December

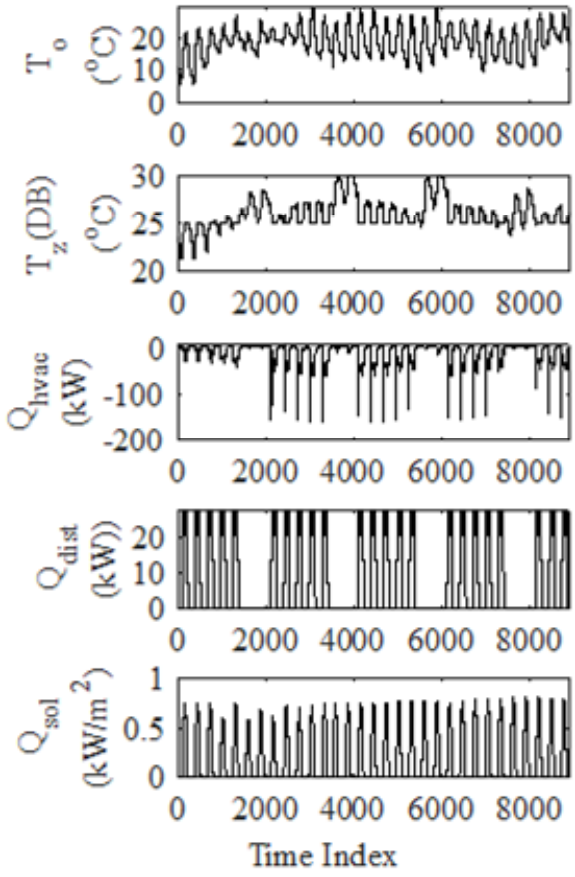

The model was simulated over two periods of one month, namely July and December, and with a simulation time step of five minutes. The two months were selected to be representative of a cold and a hot weather respectively for Port Hedland, Australia. One objective of this work was to identify models using data collected during the unforced operation of the building HVAC system. Another objective was to use the commonly available inputs, thereby requiring no additional modelling effort to obtain special inputs such as sol-air temperature and solar irradiance on facades oriented differently. Thus, Q_{sol}, Q_{hvac}, Q_{dist} and T_o were used as inputs and T_z as output, to identify the control oriented thermal models. The DesignBuilder simulation results for July are shown in Figure 2. The same disturbance profile was applied for the month of December. Figure 4 shows the model input-output data for December.

2.3 Model identification using open-loop data

All simulations were carried out in MATLAB on a Core i5 laptop having 8 GB of RAM. The optimisation and PEM methods were investigated. Data for 20 days were used for model estimation, and data for ten days were used for its validation. The optimisation aim was to fit the modelled T_z to emulator model T_z. The following factors were investigated in order to understand how to perform identification using the closed-loop data later on:

1 Five commonly employed objective functions were analysed: SSE, RMSE, MAE, mean absolute percentage error (MAPE) and sum of absolute error (SAE), as defined in equations (5)–(9).

$$SSE = \sum_{k=1}^{k=N} \left(y_{k_{actual}} - y_{k_{model}} \right)^2 \tag{5}$$

$$SAE = \sum_{k=1}^{k=N} \left| y_{k_{actual}} - y_{k_{model}} \right| \tag{6}$$

$$RMSE = \sqrt{\frac{\sum_{k=1}^{k=N} \left(y_{k_{actual}} - y_{k_{model}} \right)^2}{N}} \tag{7}$$

$$MAE = \frac{\sum_{k=1}^{k=N} \left| y_{k_{actual}} - y_{k_{model}} \right|}{N} \tag{8}$$

$$MAPE = \frac{100\%}{N} \sum_{k=1}^{k=N} \left| \frac{y_{k_{actual}} - y_{k_{model}}}{y_{k_{actual}}} \right| \tag{9}$$

where $y_{k_{actual}}$ represents the actual temperature at time k, while $y_{k_{model}}$ represents the model output at time k. N is the number of data points.

2 The objective function being a non-convex function of the parameter vector, the optimisation could lead to a local minimum, depending on the initial parameter vector guess (IPG). Therefore, 30 IPGs were generated using Latin hypercube sampling (Arroyo et al., 2020), leading to 30 optimal solutions. Different authors have used different measures such as ‘mean’, ‘median’ and ‘mode’ to obtain the plant parameters from the optimal solutions. Arroyo et al. (2020) and Blum et al. (2019) selected the optimal parameter set which led to the minimum value of the objective function during the training phase. Coffman and Barooah (2017) used the ‘mode’. The median and mean of the optimal parameter vectors might not be a wise choice when ratios linking different parameters and/or inputs have to be estimated alongside the parameters. Moreover, the optimal parameter vector associated with *P*min can be a local optimum, and thus the identified parameters can be far from the actual parameters. In this work, we investigated the effect of these choices on the identification results.

3 The effect of the parameter range was analysed. For the narrow parameter search space, each parameter was in the range of $x \pm 0.3x$, where x was the nominal parameter value provided in Section 2.1. For the wide parameter search space (Arroyo et al., 2020), all the

parameters had a minimum value of 0. The maximum values were as follows: A and B had maximum values of 160. R_e and R_{im} had maximum values of 100 K/kW. C_z and C_{im} had maximum values of 5×10^6 kJ/K.

4 To study the impact of noisy measurements, random noises having reasonable standard deviations were added to the input-output data. The standard deviations were 0.3°C for the temperatures, 0.05 kW/m^2 for the Q_{sol}, 0.5 kW for the Q_{hvac} and 0.4 kW for the Q_{dist}. These standard deviations were used to reflect the noisy measurements which can be available from relatively cheap sensors. The noisy Q_{sol} and Q_{dist} data were not allowed to contain negative values. The models identified using noisy data were subsequently simulated using clean input data, and the corresponding outputs were compared to the actual outputs.

5 To study the impact of the initial state on the estimation results, T_{im} was assumed to be 20°C in the first case (IS2) and 30°C in another case (IS3), rather than the correct value of 25°C (IS1). T_z was fixed at 25°C. MATLAB has a built-in function as part of the 'idgrey' command, to estimate the state either partially or fully every time an IPG is considered. This was additionally investigated in this work, rather than reasonably assuming the initial state. No work has been found in literature dealing with the effect of the initial state on the parameter estimation results.

6 Identification was carried out both in the presence and the absence of disturbances. Most works have neglected disturbances, while in practice there is always some unmeasured heat source affecting the zone temperature.

Identification through fitting of the modelled T_z to the actual T_z, as performed by numerous works, assumes no disturbance, which will not work in practice as unmeasured disturbances are always present. Thus, a predictive model, which estimates a disturbance is more realistic. The aim of using the PEM was to investigate if models with good multi-step ahead prediction capabilities could be identified. Analysis was initially performed for the wide parameter range and no noise conditions. The initial state was estimated within the PEM algorithm. The stability of the resulting model was set to be enforced by the algorithm. The 'fmincon' function with the 'interior-point' algorithm was used, and the maximum number of iterations was set to 1,000. Thirty IPGs were considered. The algorithm could either be set to estimate a disturbance or the latter could be set to 'none'. The impacts of these settings in the presence and the absence of unknown disturbances were investigated. The 24-hours ahead prediction accuracies were studied.

2.4 Model identification using closed-loop data from DesignBuilder

Based on the findings from the RC model identification using open-loop data (described in the results section), the closed-loop DesignBuilder data was used to estimate RC models. The optimisation, PEM and subspace + PEM identification methods were applied to the closed-loop data. The RC model developed for the closed-loop data is shown in Figure 5. A third order model was used as it takes into account the thermal capacitances of the concrete envelope (C_e), zone air (C_z) and internal mass of the zone (C_{im}) (Ferracuti et al., 2017; Blum et al., 2019; Wang et al., 2019b). The CQ_{sol} term represented the effect of solar radiation on the temperature of the envelope. The Q_{hvac} being convective, it affected the zone air only. The Q_{dist} being both convective and radiative, it affected both the internal thermal mass and the zone air, based on the parameter D. The factor α determined the interior and exterior resistances of the envelope. R_{im} represented the thermal resistance between C_z and C_{im}. All the other parameters were defined as for Figure 1. The continuous-time state-space model is shown in equations (10)–(14).

$$\begin{bmatrix} \dot{T}_z \\ \dot{T}_{im} \\ \dot{T}_e \end{bmatrix} = [A_c] \begin{bmatrix} T_z \\ T_{im} \\ T_e \end{bmatrix} + [B_c] \begin{bmatrix} T_o \\ Q_{sol} \\ Q_{hvac} \\ Q_{dist} \end{bmatrix} \tag{10}$$

$$[y] = [C_c] \begin{bmatrix} T_z \\ T_{im} \\ T_e \end{bmatrix} \tag{11}$$

$$\begin{bmatrix} -\frac{1}{R_g C_z} - \frac{1}{R_{im} C_z} - \frac{1}{(1-\alpha) R_e C_z} & \frac{1}{R_{im} C_z} & \frac{1}{(1-\alpha) R_e C_z} \\ \frac{1}{R_{im} C_{im}} & -\frac{1}{R_{im} C_{im}} & 0 \\ \frac{1}{(1-\alpha) R_e C_e} & 0 & -\frac{1}{\alpha R_e C_e} - \frac{1}{(1-\alpha) R_e C_e} \end{bmatrix} \tag{12}$$

$$[B_c] = \begin{bmatrix} \frac{1}{R_g C_z} & \frac{B}{C_z} & \frac{1}{C_z} & \frac{(1-D)}{C_z} \\ 0 & \frac{A}{C_{im}} & 0 & \frac{D}{C_{im}} \\ \frac{1}{\alpha R_e C_e} & \frac{C}{C_e} & 0 & 0 \end{bmatrix} \tag{13}$$

$$[C_c] = [1 \quad 0 \quad 0] \tag{14}$$

The values of the individual model parameters could not be determined accurately, such that a narrow parameter search space would not be beneficial. Moreover, an initial parameter identification using a narrow search space led to an unphysical model having a poor simulation RMSE. Therefore, a wide parameter range was subsequently chosen as follows. A: 0–300 m^2, B = 0–60 m^2, C = 0–2,000 m^2, (α, D): 0–1, (R_e, R_{im}, R_g): 0–10 K/kW, (C_z, C_{im}, C_e): 0–3 $\times$ 10^6 kJ/K.

For the PEM method, the initial state and the disturbance model were set to be estimated by the PEM algorithm. The model stability was enforced during the

identification. The search method was set to 'fmincon', the algorithm was selected as 'interior-point' and the maximum number of iterations was set to 1,000.

Figure 5 RC model for DesignBuilder data

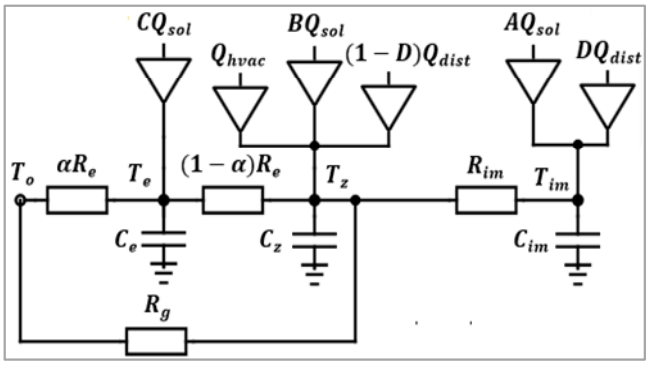

For the subspace identification (Privara et al., 2012), the 'N4SID' algorithm, in MATLAB System Identification Toolbox was used to identify the discrete-time LTI black-box state-space model shown by equations (15) and (16).

$$x_{k+1} = A_d x_k + B_d u_k + K_d e_k \tag{15}$$

$$y_k = C_d x_k + e_k \tag{16}$$

State-space matrices A_d, B_d, C_d and disturbance matrix K_d were estimated by the algorithm. u_k was the input vector comprising $T_z(k)$, $Q_{sol}(k)$, $Q_{hvac}(k)$ and $Q_{dist}(k)$. y_k was the output $T_z(k)$. e_k was the disturbance to be estimated and x_k was the state vector. The stability of the identified model was selected to be enforced by the algorithm. The canonical variate algorithm was used as the weighting scheme for the singular-value decomposition by the N4SID algorithm. A third order model was selected (Prívara et al., 2013) as higher order models did not bring much improvement in the results. The Hankel matrix size was varied between 10 and 70 and was selected to be 40 based on the trade-off between the 24-hours ahead prediction accuracy, and the autocorrelation and cross-correlation of residuals (Joe and Karava, 2017). The disturbance model was set to be estimated by the algorithm. Subspace identification was also performed in the presence of noise in the identification data, whereby the noise levels reported in Section 2.3 were added to the input and output data, in order to represent noisy measurements available from cheap sensors. When the disturbance was assumed to be partially known, the same disturbance noise level was considered as for the case when the disturbance was fully known. The estimated models were then refined through PEM and subsequently validated using data without noise, and the resulting output was compared to the noiseless zone temperature data obtained from DesignBuilder. This comparison would be useful to know how the predictions by estimated model differ from the actual zone temperature. The ability of the identified models to perform 5 min to 24-hours ahead predictions were quantified for both July and December and for all cases (unknown disturbances, noisy data). One important analysis which has been ignored in most works dealing with the development of prediction models for MPC of building HVAC systems is about the autocorrelation and cross-correlation of the model residuals. If the residuals are highly correlated, the models can be improved in order to have a better prediction. Therefore, a good model should have the residual autocorrelation function inside the confidence interval of the corresponding estimates (MathWorks, 2021). Moreover, a good model is supposed to have residuals which are uncorrelated with past inputs. Any correlation indicated by a peak outside the confidence interval at a certain lag implies that the output has not been described by the input at that lag. This aspect was thoroughly investigated in this work. The performance indicators used to assess the suitability of the models are shown in equations (7), (8) and (17)–(19). The Theil's inequality coefficient (TIC) (Fang and Lahdelma, 2016; Bnhamdoon et al., 2020) takes a value between 0 and 1, where 0 indicates a perfect prediction, and 1 indicates that the prediction is no better than a naïve guess. Generally, when $TIC < 0.25$, the prediction of the estimated model is considered acceptable (Guo et al., 2017; Bnhamdoon et al., 2020).

$$R^2 = 1 - \frac{\sum_{k=1}^{k=N} \left(y_{k_{actual}} - y_{k_{model}} \right)^2}{\sum_{k=1}^{k=N} \left(y_{k_{actual}} - \frac{1}{N} \sum_{k=1}^{k=N} \left(y_{k_{actual}} \right) \right)^2} \tag{17}$$

$$PAE = \max \left(abs \left(y_{k_{actual}} - y_{k_{model}} \right) \right) \tag{18}$$

$$TIC = 1 - \frac{\sqrt{\frac{1}{N} \sum_{k=1}^{k=N} \left(y_{k_{actual}} - y_{k_{model}} \right)^2}}{\sqrt{\frac{1}{N} \sum_{k=1}^{k=N} \left(y_{k_{actual}} \right)^2} + \sqrt{\frac{1}{N} \sum_{k=1}^{k=N} \left(y_{k_{model}} \right)^2}}. \tag{19}$$

2.5 Model identification using experimental data from a real building

The experimental data was collected from a large auditorium shown in Figure 6. The building has an occupied area of around 540 m^2 and is located on the University of Florida Campus. The thermal zone is serviced by a dedicated air handling unit, and a proportional-integral controller is used to control Q_{hvac} so that the room temperature tracks a set-point. T_a was obtained from weatherunderground.com, Q_{sol} was collected from the National Solar Radiation Database. Q_{hvac} was computed from measurements of supply air flow rate, temperature of supplied air, and temperature of return air. Latent heat was ignored so that the calculated Q_{hvac} was accurate only when there was not much difference between the supply and return duct humidities. A thermostat in the building was used to measure T_z. The CO_2 concentration of the auditorium was also measured in the return duct. All the data was collected during the normal operation of the building, when the HVAC system was under closed-loop control, i.e., no persistently exciting identification data was

generated. Measurements were carried out over two periods of 14 days each, in summer and in winter. Data for the first ten days were used for model estimation, and data for the last four days were used for the model validation, for each of the considered cases (summer, winter, no Q_{sol}). The size of the Hankel matrix was pre-determined to be 25, and a third order model was found to be appropriate. Coffman and Barooah (2017) reported the identification of an RC grey-box model alongside the unmeasured disturbances using the same data, but the estimated R and C parameters could not be discussed due to lack of ground truth. Therefore, in this work, the experimental data was used to estimate only the linear black-box model, in an attempt to validate the performance of the N4SID + PEM method. Coffman and Barooah (2017) also reported a good correlation between the measured CO_2 concentration and the estimated disturbances. Therefore, in this work, the CO_2 concentration was used as an input representing the disturbances in the zone.

Figure 6 Experimental building (see online version for colours)

3 Results and discussion

3.1 Analysis on open-loop data (generated by the known second model in Figure 1)

3.1.1 Effect of the objective function – optimisation technique

Figure 7 shows the training (T) and validation (P) RMSEs for the models identified using noiseless data. The results associated with the different objective functions (SSE, MAE, MAPE, RMSE and SAE) are presented. The results associated with the different initial states of IS1, IS2 and IS3 are also shown as numbers 1, 2 and 3, respectively. For instance, SSE2 implies that the objective function was the SSE and the initial state was IS1. Moreover, the results are also shown for the different ways of determining the identified model from the 30 optimal parameter vectors. *T*mean and *P*mean correspond to the model whose parameters were set as the mean of the 30 optimal solutions. *T*median and *P*median correspond to the model whose parameters were set as the median of the 30 optimal solutions. *T*min and *P*min correspond to that optimal parameter vector out of the 30 optimal solutions, which led to a model with the minimum training RMSE. For the initial state IS1, the identified models produced the lowest RMSEs. Thus, wrongly assuming an initial state degrades the performance of the resulting model. For the IS1 cases, the SSE and RMSE objective functions led to models with similar and the lowest simulation RMSEs, as compared to the other objective functions. The RMSE objective function was used by Cui et al. (2019) and Delcroix et al. (2020), while the SSE objective function was used by Blum et al. (2019). *P*median and *P*min had RMSE values of the order of 10^{-7} for the SSE1, RMSE1 and SAE1 cases while *P*mean had much higher RMSE values, implying that the mean of the optimal parameter vectors is not a good choice for the identified parameter vector.

Figure 7 Impact of different objective functions, different measures and initial states (see online version for colours)

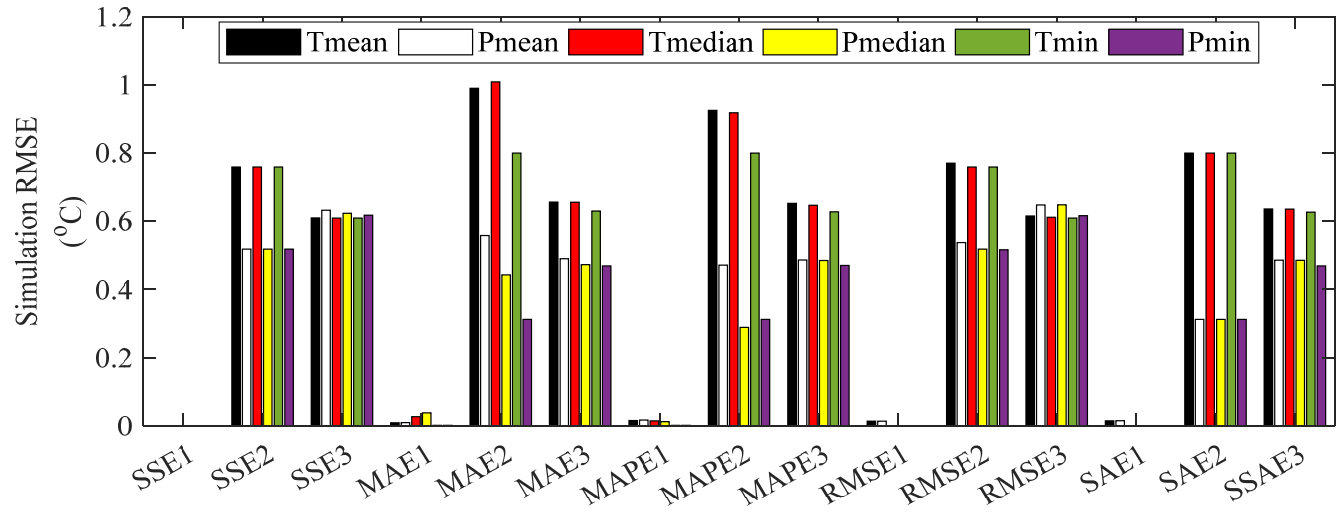

Figure 8 Impact of the size of the parameter search space (see online version for colours)

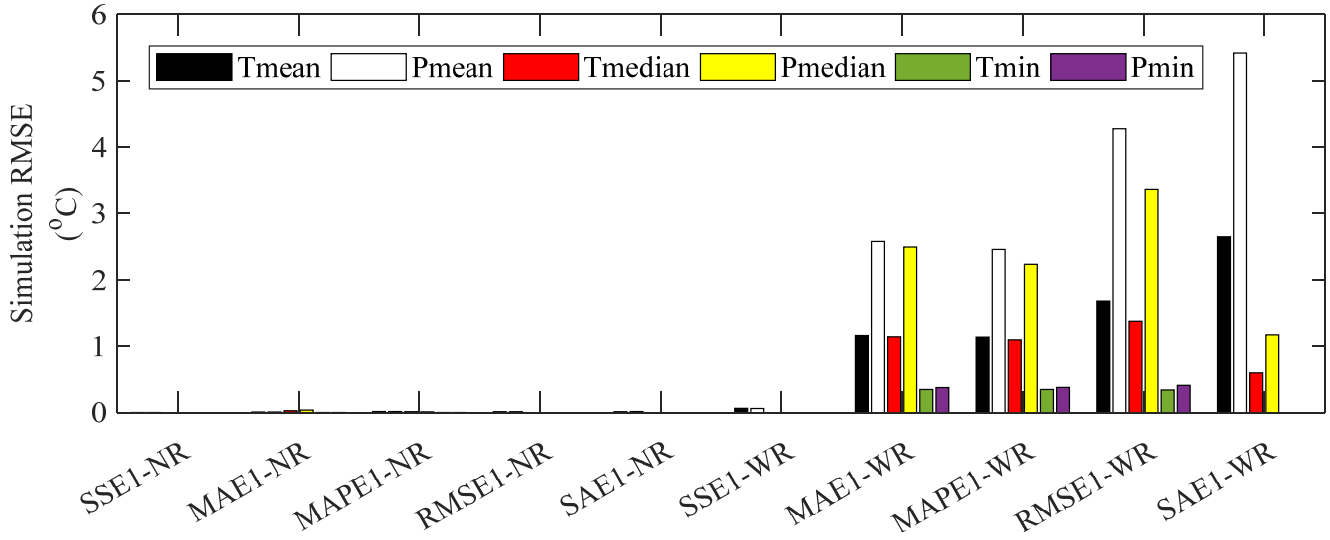

Note: WR: wide range and NR: narrow range.

3.2 *Effect of the size of the parameter search space – optimisation technique*

Figure 8 shows the training and validation RMSEs for models identified using both the narrow and wide parameter ranges. The SSE objective function led to the best performance for the wide parameter range, with RMSEs for *P*median and *P*min being of the order of 10^{-7}. The SAE objective function led to a model with an RMSE for *P*min of the order of 10^{-7}, but the *P*median was relatively higher. For the other objective functions, *P*median and *P*mean were much higher than *P*min. Such differences between *P*median, *P*mean and *P*min were not observed for the narrow parameter range case. Thus, for wide parameter ranges, the best model is obtained as the one with the lowest *T*min, as considered in Blum et al. (2019). However, this does not guarantee that the optimal parameter vector will be physically meaningful.

Figure 9 shows the box-whisker plots for the parameters identified using the narrow parameter range. The identified parameters were normalised to their corresponding true values. The longer horizontal bar represents the normalised medians. The shorter horizontal bars represent the normalised minimum and maximum values of the parameters. The box represents the first quartile to the third quartile. The '+' are the outliers, defined in this case as a value, which is more than 1.5 times the interquartile range away from the top or bottom of the box. Ideally, the best result should be just the median line located exactly at 1, with no box and with no outlier.

As can be observed, the parameters identified through the SSE objective function were more accurate without any outlier, as compared to the other objective functions. The box plots for the parameters identified using the RMSE and the SAE objective functions were very similar. The parameters identified using the MAE and the MAPE objective functions were more scattered over the search space. Figure 9(e) and Figure 9(f) show that the parameters identified were inaccurate when the initial state was wrong, even though the SSE objective function was used. Figure 10 shows the box plots for the wide parameter search space. It can be observed that the SSE objective function led to more accurate parameters as shown in Figure 10(d).

Figure 9 Box plots – narrow parameter range analysis for (a) MAE1, (b) MAPE1, (c) RMSE1 (SAE1 similar), (d) SSE1, (e) SSE2 and (f) SSE3 (see online version for colours)

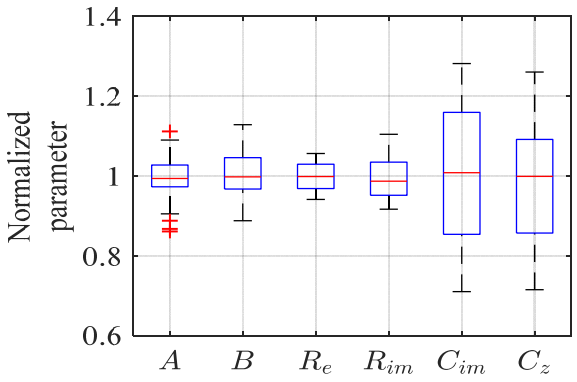

(a)

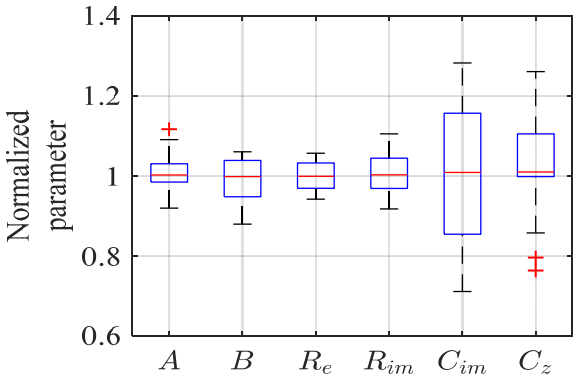

(b)

Figure 9 Box plots – narrow parameter range analysis for (a) MAE1, (b) MAPE1, (c) RMSE1 (SAE1 similar), (d) SSE1, (e) SSE2 and (f) SSE3 (continued) (see online version for colours)

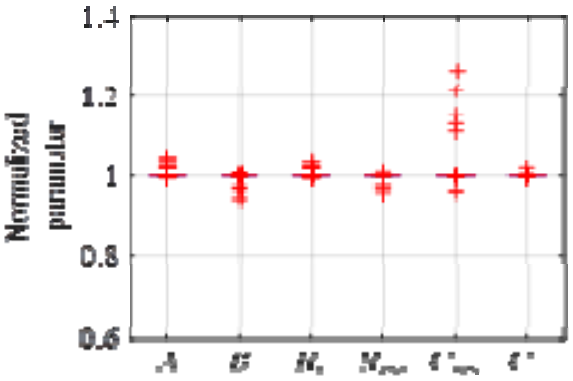

(c)

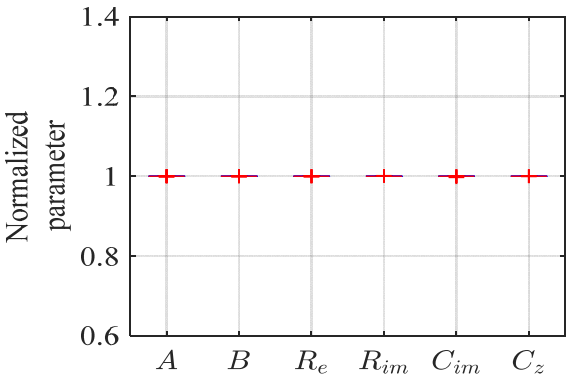

(d)

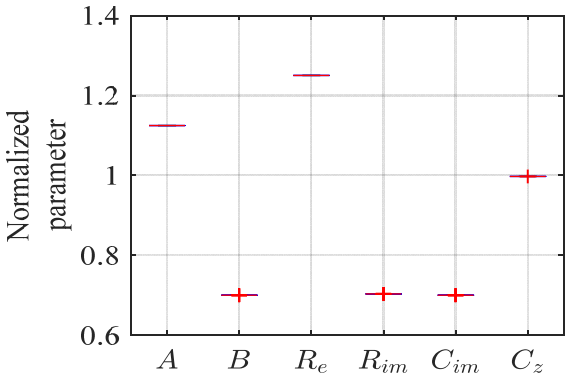

(e)

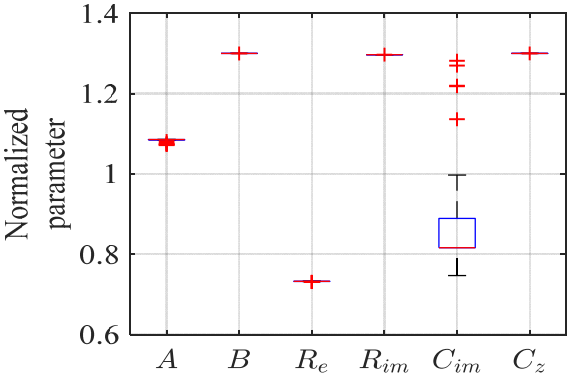

(f)

Figure 10 Box plots – wide parameter range analysis for (a) MAE1 (RMSE1 similar), (b) MAPE1, (c) SAE1, (d) SSE1, (e) SSE2 and (f) SSE3 (see online version for colours)

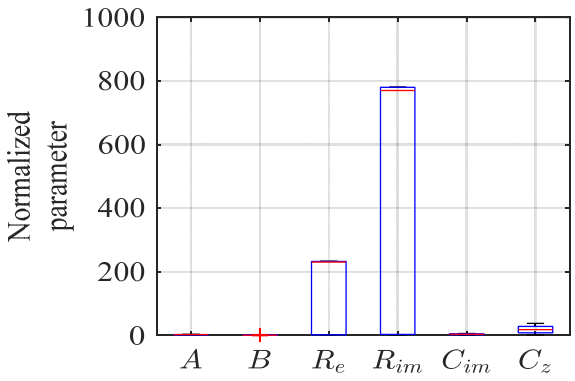

(a)

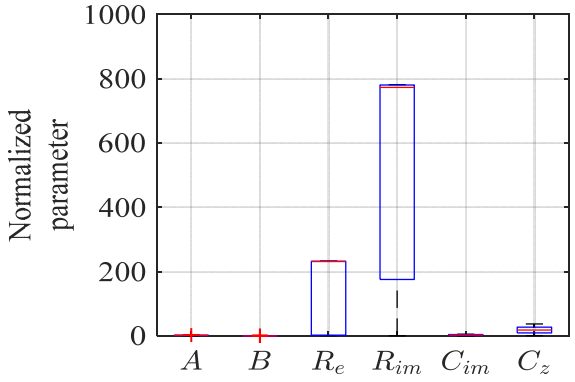

(b)

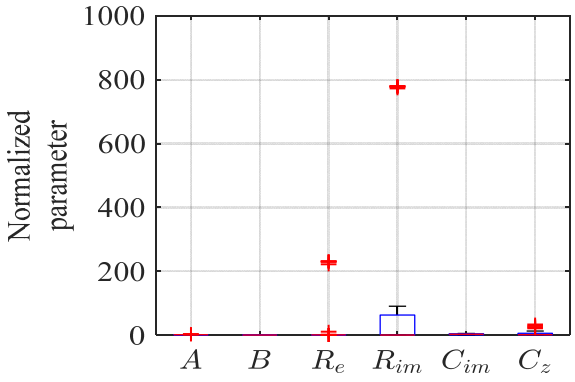

(c)

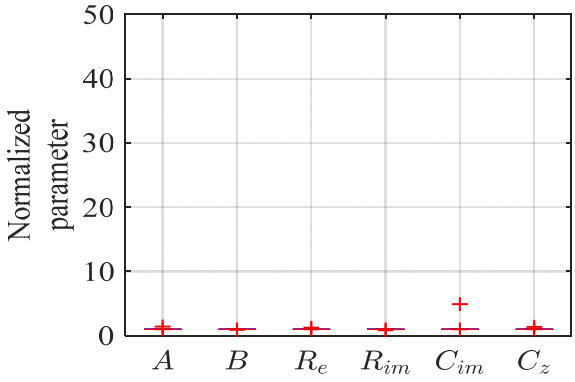

(d)

Figure 10 Box plots – wide parameter range analysis for (a) MAE1 (RMSE1 similar), (b) MAPE1, (c) SAE1, (d) SSE1, (e) SSE2 and (f) SSE3 (continued) (see online version for colours)

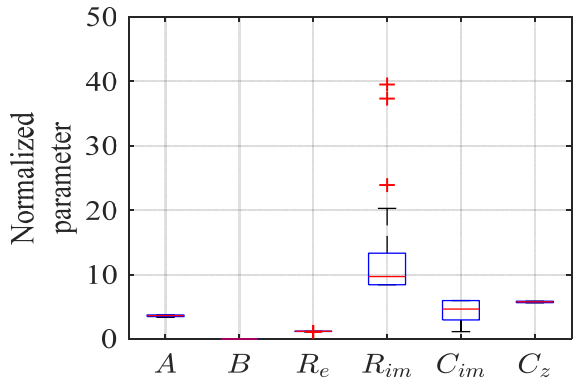

(e)

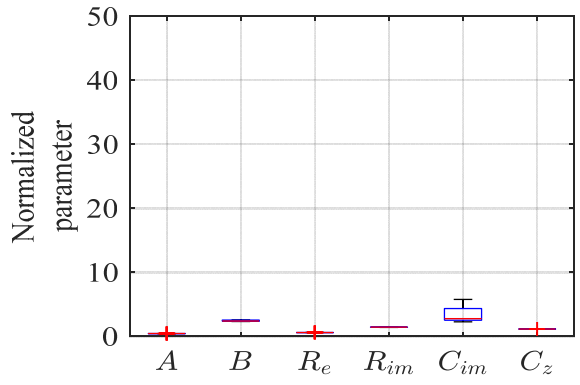

(f)

Compared to Figure 9, the MAE and MAPE objective functions led to an even worst model under the wide parameter range conditions, as depicted by the scattering of the identified parameters, especially R_e, R_{im} and C_z, over a large range [Figure 10(a) compared to Figure 9(a), Figure 10(b) compared to Figure 9(b)]. Similarly, the models identified using the wrong initial state were even worse under wide parameter range conditions [Figure 10(e) compared to Figure 9(e), Figure 10(f) compared to Figure 9(f)].

3.2.1 Effect of noisy identification data – optimisation technique

Figure 11 shows the box plots for the parameters identified using noisy data for the different objective functions under the narrow parameter search space condition.

The SSE objective function produced the best results, with no outlier and with the parameters being scattered over narrower range, as compared to the other objective functions. Comparing Figure 11(d) to Figure 9(d), it can be deduced that the noisy data affected the optimisation-based identification by scattering the identified parameters over a wider range. Figure 12 shows the standard deviation of the noise in the input/output data for the 32 input/output combinations. Figure 12 additionally shows the corresponding validation RMSE for the model identified under each noise combination. The variation in the RMSEs were similar to the variation of the standard deviation in the GHI. Blum et al. (2019) reported similar findings. The *P*median and *P*mean RMSEs for the different objective functions are not shown on Figure 12, but they had very similar values to the *P*min RMSEs. Moreover, comparing Figure 12 to Figure 7, it can again be deduced that the noisy identification data led to a model having a worse simulation RMSE than one identified using noiseless data.

Figure 11 Box plots – noisy identification data – narrow parameter range for (a) MAE1 (MAPE1 similar), (b) RMSE1, (c) SAE1 and (d) SSE1 (see online version for colours)

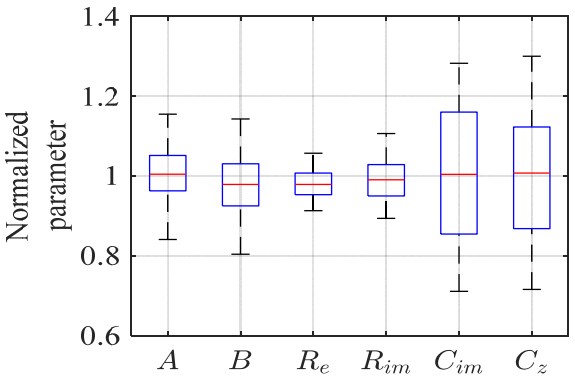

(a)

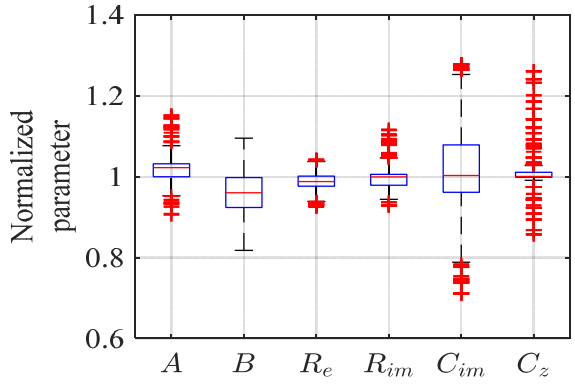

(b)

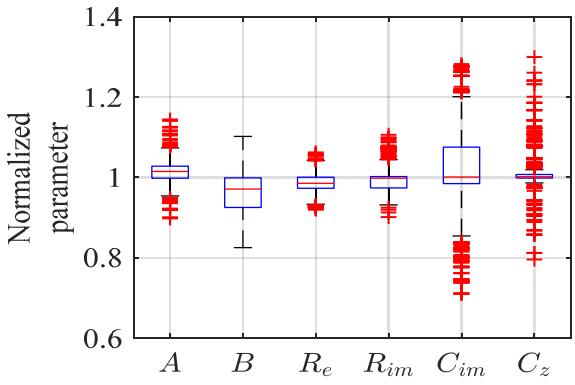

(c)

Figure 11 Box plots – noisy identification data – narrow parameter range for (a) MAE1 (MAPE1 similar), (b) RMSE1, (c) SAE1 and (d) SSE1 (continued) (see online version for colours)

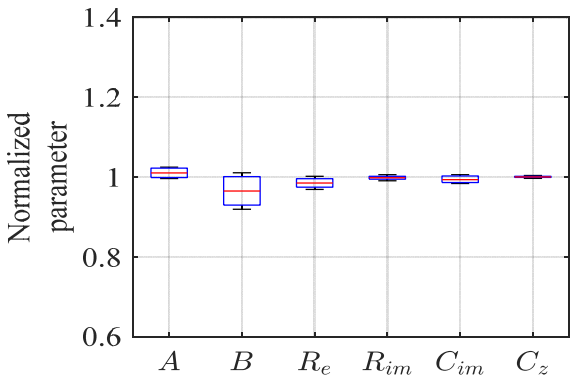

(d)

3.2.2 *Estimating the initial state prior to identification – optimisation technique*

The wrong initial state affected the accuracy of the identified model as reported in Section 3.1.1. Therefore, the initial second state T_{im} was partially estimated in this work, prior to performing the identification for each IPG. Figure 13 shows the resulting box plots for the narrow and wide parameter ranges. Comparing Figure 13(a) to Figure 9(e) and Figure 9(f) for the NR condition, a significant improvement can be seen in the results, when the initial state was estimated. Similarly, comparing Figure 13(b) to Figure 10(e) and Figure 10(f) for the WR condition, it can be deduced that estimating the initial state prior to the parameter identification resulted in more accurate models, given that the normalised median parameters were closer to 1. Such results have not been reported in any work dealing with optimisation-based identification of grey-box RC models.

Figure 14 compares the validation results for different ways of considering the initial state. One immediate observation is that the RMSEs were the smallest when the initial state was known exactly. When the initial state was incorrect, however, the RMSEs became much larger. When the initial state was estimated prior to performing the optimisation, the simulation RMSEs improved slightly when the parameter search space was narrow, but remained relatively high when the search space was wide. After estimating the initial state for each IPG, 30 optimal parameter sets were obtained. The initial state was again estimated for each optimal solution, after which the models were validated again. This process was found to significantly improve the simulation RMSEs when the parameter search space was wide. No visible improvement, however, occurred for the narrow parameter range. This technique can be employed for optimisation-based identification cases where the initial state is not known accurately.

3.2.3 *Estimating the initial state prior to identification – optimisation technique*

Figure 15 shows the box plots resulting from the identification process when Q_{dist} was assumed unknown so that it was not used in the optimisation process. However, it had an effect on the simulated zone temperature. The initial state was set to its true value of [23.5, 25] for this analysis.

Comparing Figure 15(a) to Figure 9(d), it can be observed that the presence of an unknown disturbance shifted the median parameters away from the value of 1. Comparing Figure 15(b) to Figure 15(a), the wide parameter range scenario identified the parameters as being slightly more scattered as compared to the narrow parameter range case. Moreover, the median parameters were slightly different, with a few outliers. Thus, disturbances not accounted for during the identification process affect the estimated parameters.

Figure 12 Validation RMSEs and corresponding noise standard deviations (see online version for colours)

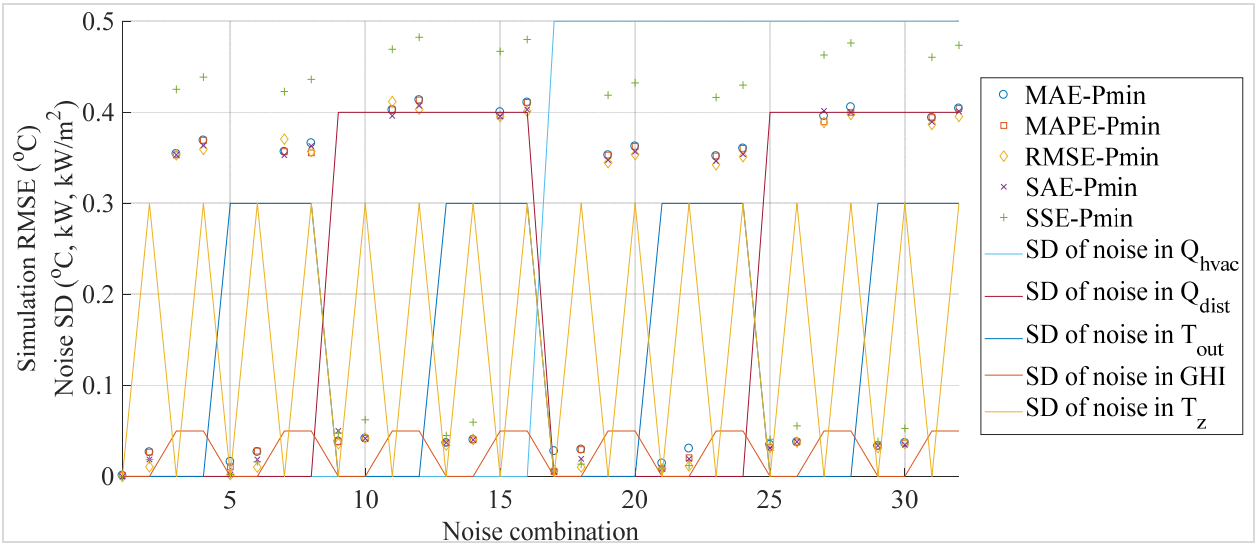

Figure 13 Box plots – state estimation prior to identification for (a) narrow parameter range and (b) wide parameter range (see online version for colours)

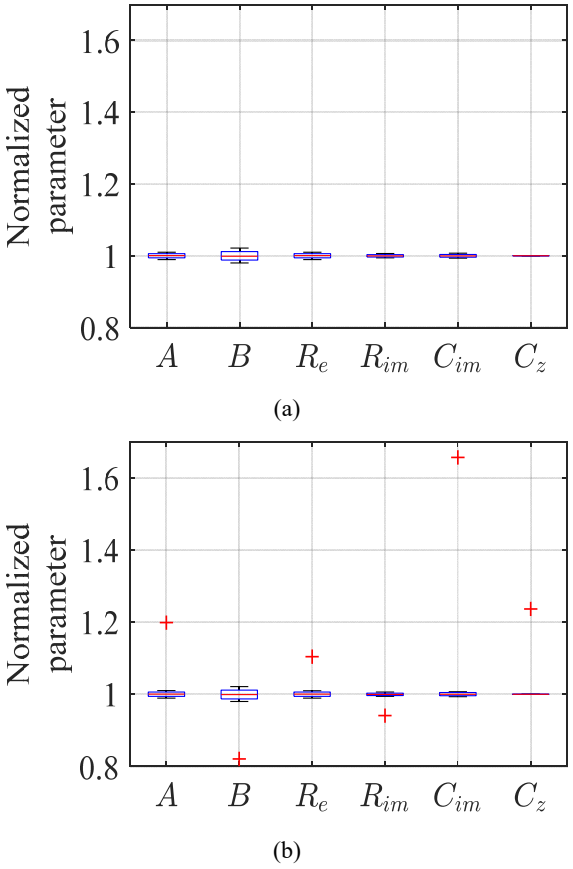

3.2.4 *Identification in the presence and absence of disturbances – PEM technique*

Figure 16(a) shows the box plot of the parameters identified using the PEM, when there was no unknown disturbance but the disturbance model in the PEM algorithm was set to 'none' (referred to as no disturbance). It can be observed that the estimated R_e and R_{im} values were not physically meaningful. When the occupancy was actually unknown, and the disturbance model in the algorithm was set to 'none' (referred to as no disturbance model), the box plot was almost the same. However, when the occupancy was unknown, and the disturbance model in the algorithm was set to 'estimate' (referred to as disturbance model), the box plot in Figure 16(b) was obtained. A slight improvement can be observed, as the medians of the normalised R_e and R_{im} are about half of those in Figure 16(a). The 24-hours ahead prediction RMSEs and peak absolute errors (PAEs) are shown in Figure 17. The RMSEs being less than 2°C implies that the model would be amenable in an MPC framework (Radecki and Hencey, 2017). The PAEs were generally quite high. It has to be noted that although the estimation of a disturbance model improved some of the identified parameters, the prediction RMSEs became worse for some IPGs, and the prediction PAEs became worse for all IPGs.

Figure 14 Validation RMSEs – initial state consideration for (a) narrow parameter range and (b) wide parameter range (see online version for colours)

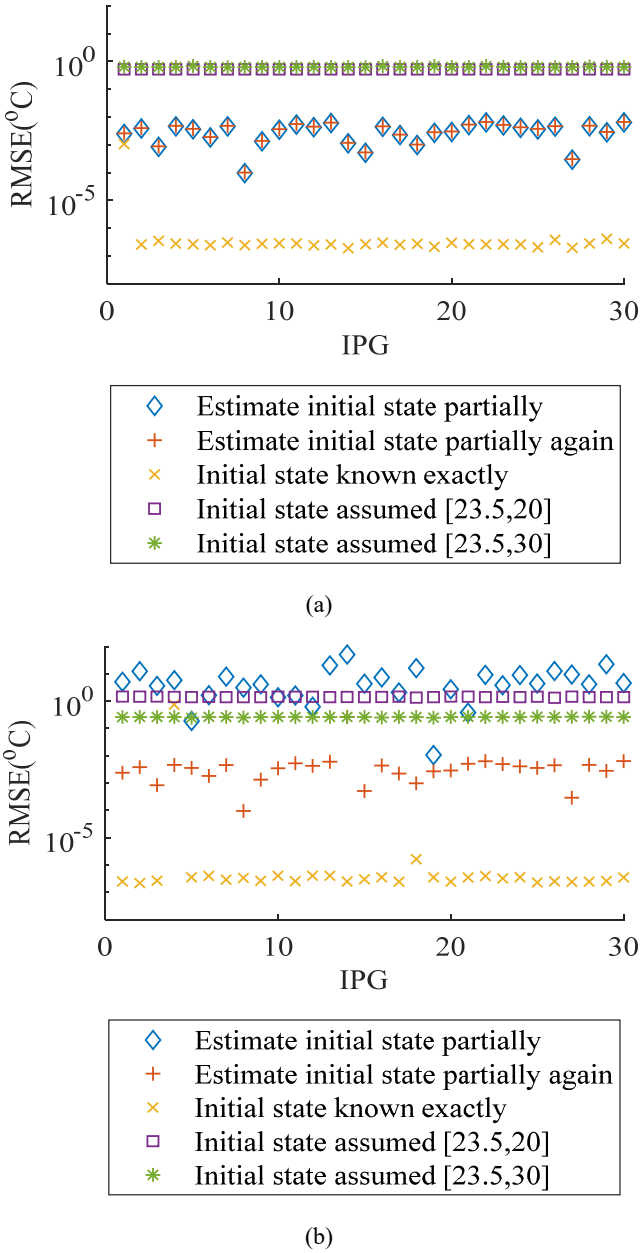

3.3 *Analysis on closed-loop data generated by DesignBuilder*

3.3.1 *Optimisation method*

The analyses on the open-loop data concluded that the SSE objective function should be used for optimisation-based identification. Moreover, it was found that the initial state should be estimated prior to performing the identification. Furthermore, it was found that the optimal parameter set should be the one resulting in the minimum training error. The box plots for the closed-loop analyses were obtained by normalising the identified parameters with respect to the parameter range, given that the true values of the parameters were unknown. Figure 18 shows the validation RMSEs of the identified models. Figure 18 also shows the box plots of

the normalised identified parameters for the following three scenarios: undetrended data for July, detrended data for July and detrended data for December. Figure 18(a) shows that detrending of the input-output data enabled the identification of models which had better validation RMSEs and PAEs.

Figure 15 Box plots – presence of unmeasured disturbances for (a) narrow parameter range and (b) wide parameter range (see online version for colours)

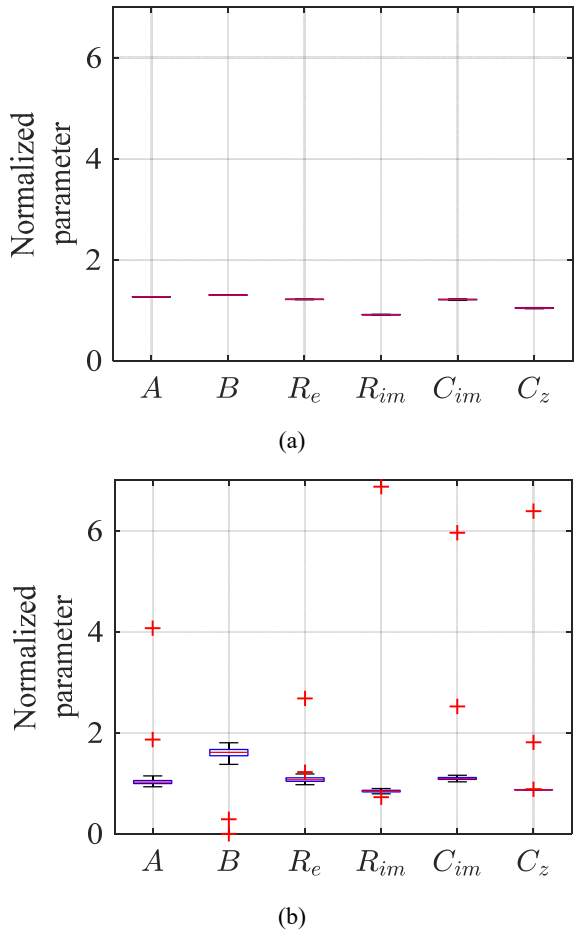

Figure 16 Box plots – PEM identification for (a) no disturbance and (b) disturbance model (see online version for colours)

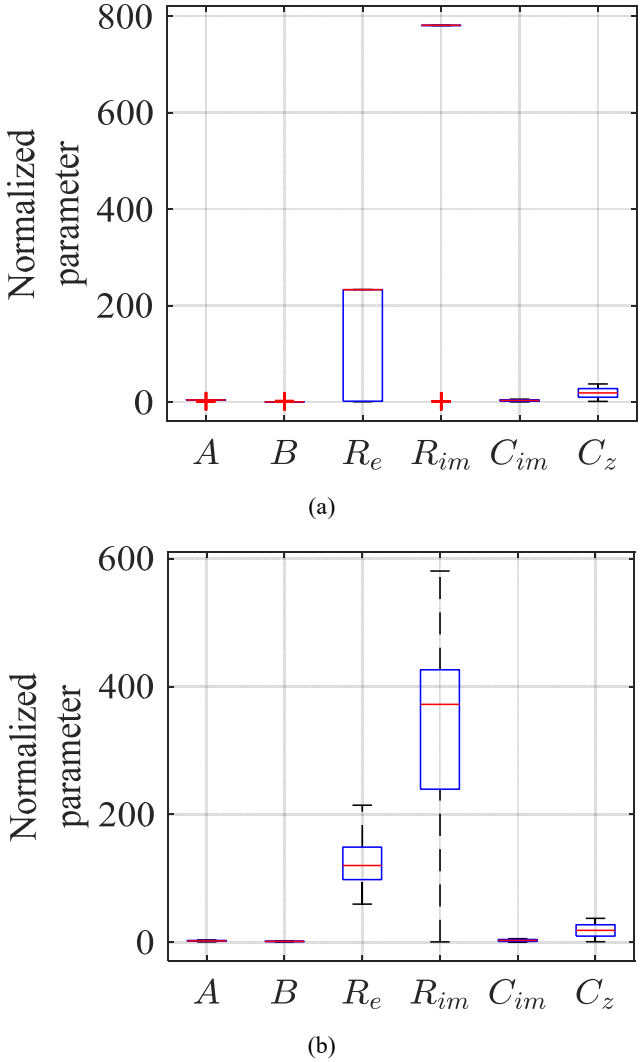

Figure 17 Prediction PAEs and RMSEs for identification by PEM algorithm (see online version for colours)

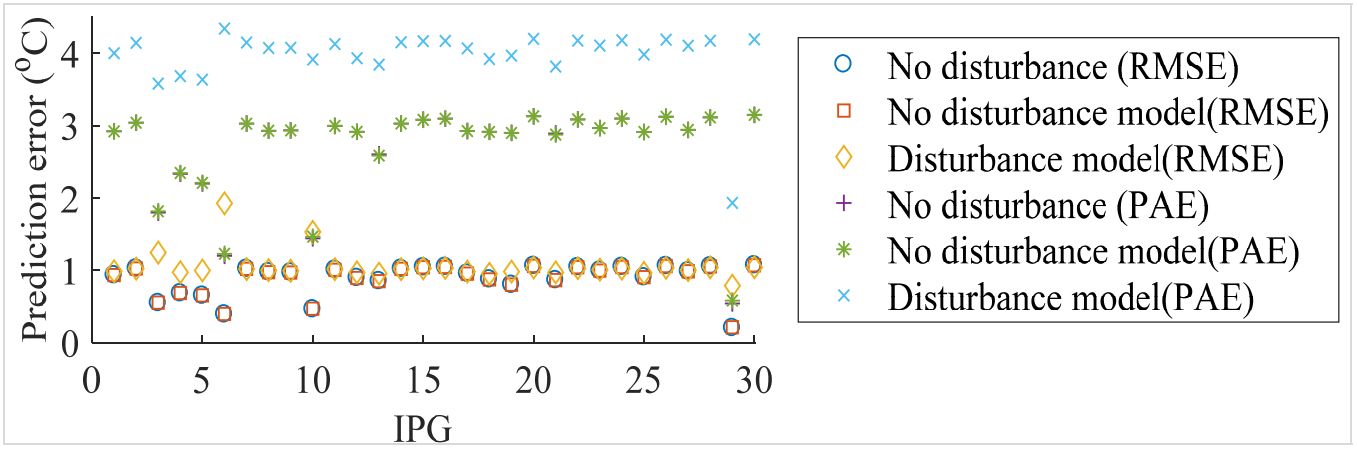

Figure 18 (a) Validation RMSEs and PAEs and box plots for closed-loop data using optimisation method for (b) July – undetrended, (c) July – detrended and (d) December – detrended (see online version for colours)

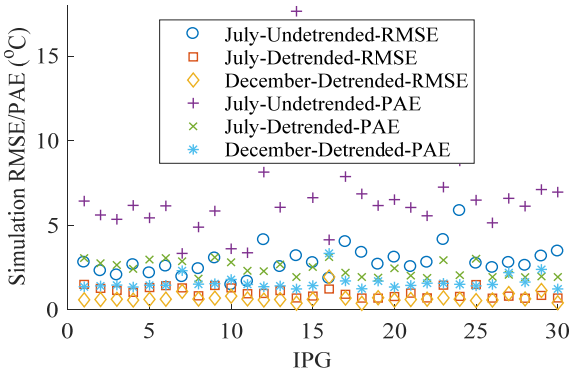

(a)

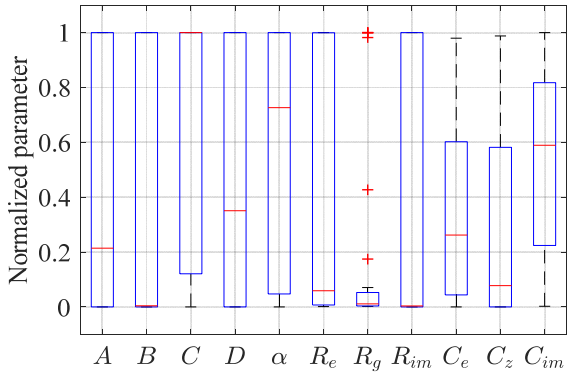

(b)

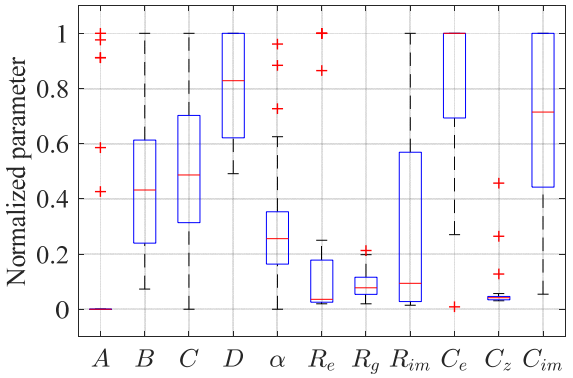

(c)

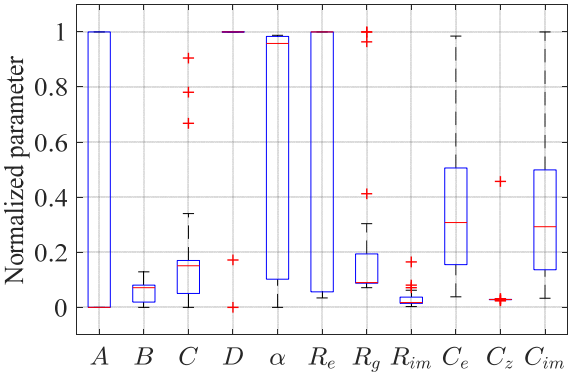

(d)

The identified model for December had a better validation performance than that for July. The variation of the RMSE was similar to that of the PAE for the same scenario. Comparing Figure 18(b) to Figure 18(c), it can be deduced that the detrending process identified the parameters such that they were spread over a narrower range. The detrended data led to most identified parameters being different from those identified using undetrended data. Comparing Figure 18(c) to Figure 18(d), it can be observed that most parameters were identified such that they were different for December, as compared to July. Thus, such parameters might not be physically meaningful, as physical parameters cannot change drastically over a time period of six months. It could be that the data was not persistently exciting. However, the 'advice' command in MALAB suggested that the data could be used to identify a very high order model. Moreover, it could be possible that the chosen model structure and the associated inputs were not appropriate to capture the prevailing thermal dynamics. However, prior to the selection of the model structure employed in this work, several other structures of varying complexities (first to third orders) were tested by trial and error and their performances were worse. A higher order model with a more complex structure was not considered, as it would be computationally demanding to be identified for a single thermal zone. The identification of each model through the optimisation method took about three hours, which is significantly high, for a single-zone building model having only 11 parameters. For all the 30 IPGs, the minimum validation RMSEs were 0.7°C, 1.46°C and 0.4°C, and the PAEs were 1.8°C, 3.3°C and 1.2°C for the July-detrended, July-undetrended and December-detrended cases, respectively. Therefore, even though the identified parameters were not physically meaningful, a third order model capable of reproducing the thermal dynamics of a single zone with sufficient accuracy was developed and identified in this work.

Figure 19 Box plots – closed-loop identification data using PEM method for (a) July – detrended and (b) December – detrended, (c) prediction RMSEs and (d) prediction PAEs (see online version for colours)

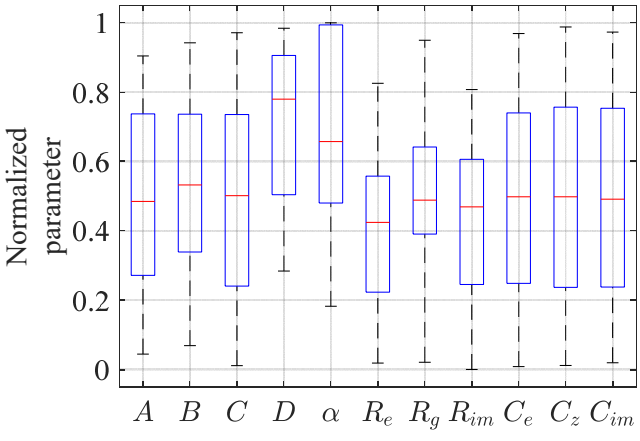

(a)

Figure 19 Box plots – closed-loop identification data using PEM method for (a) July – detrended and (b) December – detrended, (c) prediction RMSEs and (d) prediction PAEs (continued) (see online version for colours)

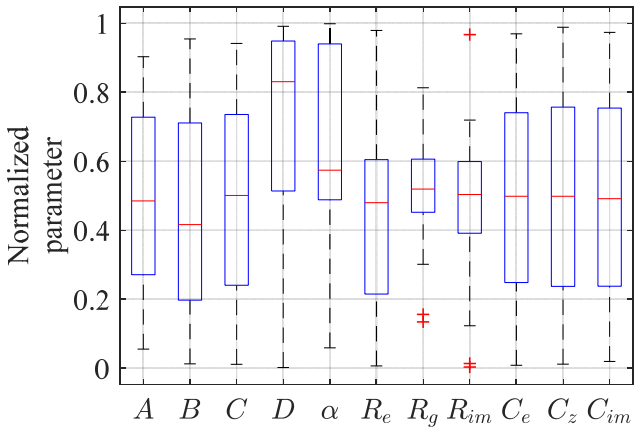

(b)

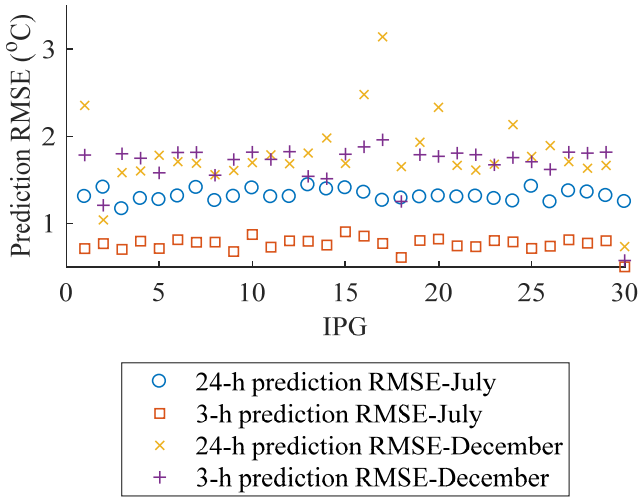

(c)

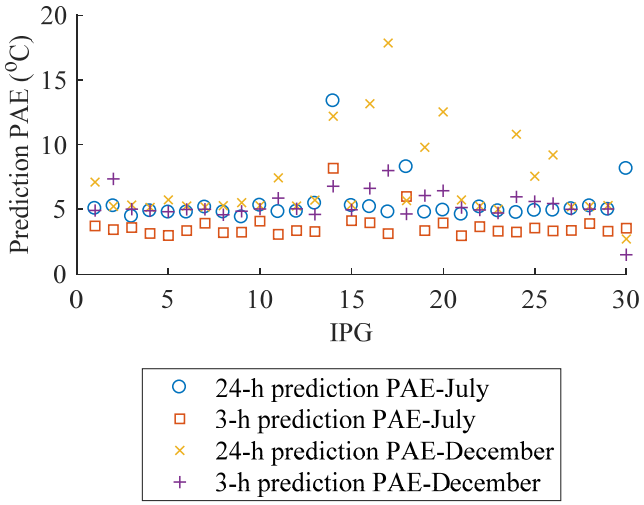

(d)

3.3.2 PEM method

The box plots for the normalised identified parameters for the 30 IPGs, as well as the prediction RMSEs and PAEs are shown in Figure 19. The first observation from the box plots is that most parameters were identified as being scattered over a WR. Moreover, the identified parameters were different for July and December. Figure 19(c) shows that for most of the IPGs, the prediction RMSEs were within a range (less than 2°C) acceptable for predictive control (Radecki and Hencey, 2017). Figure 19(d) shows that the PAEs, however, were quite high. The minimum 24-hours ahead prediction PAEs were 4.4°C and 2.7°C for July and December, respectively. The time taken to identify all the models for the 30 IPGs was around 20 minutes, which is not insignificant.

3.3.3 Subspace + PEM estimation method

Figure 20–Figure 22 presents the subspace identification results. Figure 20(a) shows the 5-mins, 1-hour, 6-hours, 12-hours and 24-hours ahead predicted temperatures alongside the actual temperature for the validation dataset. The same legend is applicable for all the graphs showing similar information for all the analysed cases. It can be observed that model was able to predict the thermal dynamics accurately over the different prediction horizons. Figure 20(b) and Figure 20(c) show the autocorrelation of residuals for the N4SID estimation and N4SID + PEM estimation, respectively. The greyed region shows the 99% confidence limits. The refining of the initial N4SID model through PEM was found to improve the correlations to an acceptable level. Figure 20(d) shows the cross-correlation of residuals for the N4SID + PEM estimation, and confirms that the model was well identified. Figure 21 shows similar information as Figure 20, but for the month of July. Similar conclusions can be drawn about the performance of the estimated model as well as the training of the model, as for December. Prediction and residual analysis plots for the presence of unknown heat gains (occupancy and equipment) are not provided due to space limitations, but were acceptable and similar to Figure 20 and Figure 21. Figure 22 shows the residual analysis when noisy data was used for the identification. The results show that the models were better estimated, compared to noiseless data identification. Table 2 shows the performance metrics of the models resulting from the N4SID + PEM estimation. All the estimated models had acceptable prediction accuracies, both on the training and validation datasets, even with noisy identification data and the presence of significant unknown disturbances. The PAE is not often analysed in other works, but here is it shown that the validation prediction PAE had a maximum value of only 1.5°C. The RMSE and MAE were acceptable as well. For instance, Bäumelt and Dostál (2020) reported an MAE of up to 0.6°C. Similarly, Brastein et al. (2018) reported an RMSE of up to 1.5°C. Viot et al. (2018a) reported the best MAE of 0.73°C and PAE of around 3°C, and successfully used the model in MPC framework (Viot et al., 2018b).

Figure 20 Subpsace results for December when all the inputs were used, (a) prediction v/s actual temperatures for validation dataset (b) autocorrelation of residuals (N4SID only) (c) autocorrelation of residuals (N4SID + PEM) (d) cross-correlation of residuals (N4SID + PEM) (see online version for colours)

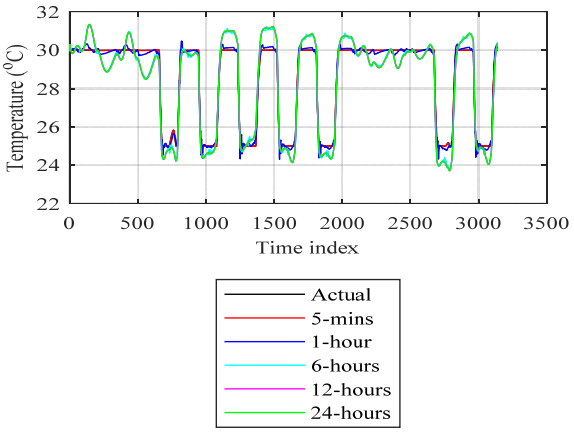

(a)

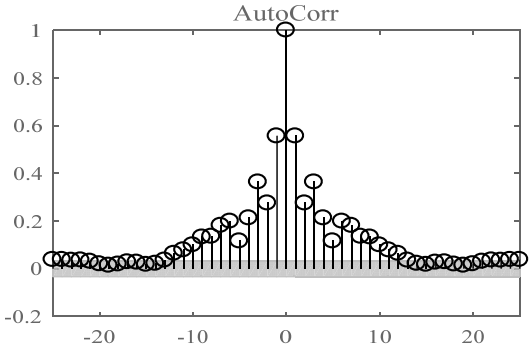

(b)

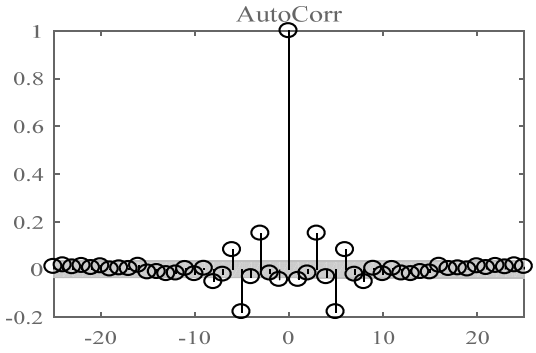

(c)

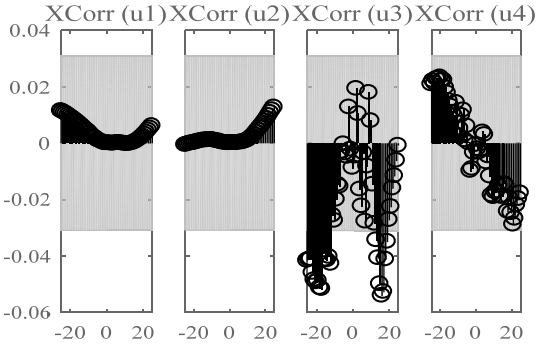

(d)

Figure 21 Subpsace results for July when all the inputs were used, (a) prediction v/s actual temperatures for validation dataset (b) autocorrelation of residuals (N4SID only) (c) autocorrelation of residuals (N4SID + PEM) (d) cross-correlation of residual (N4SID + PEM) (see online version for colours)

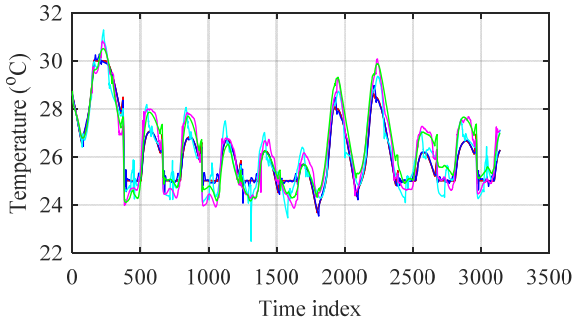

(a)

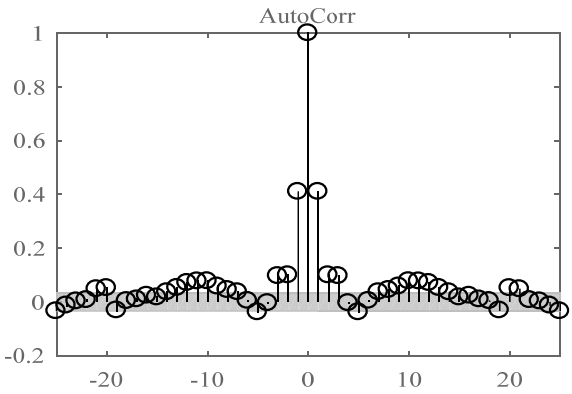

(b)

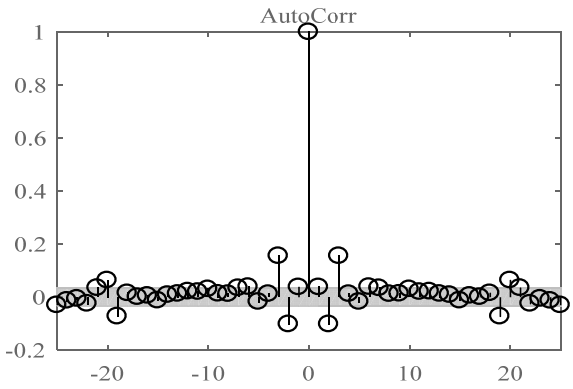

(c)

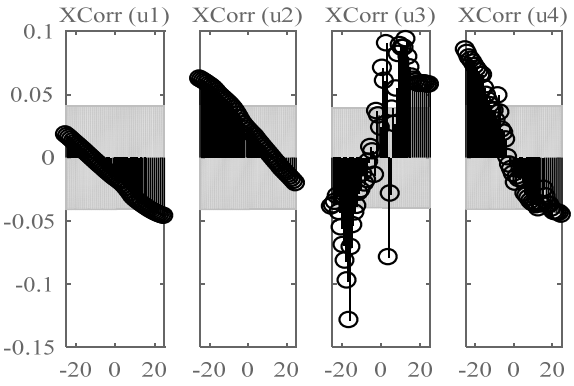

(d)

Figure 22 Residual analysis for identification using noisy data (N4SID + PEM), (a) autocorrelation – December (b) cross-correlation – December (c) autocorrelation – July (d) cross-correlation – July

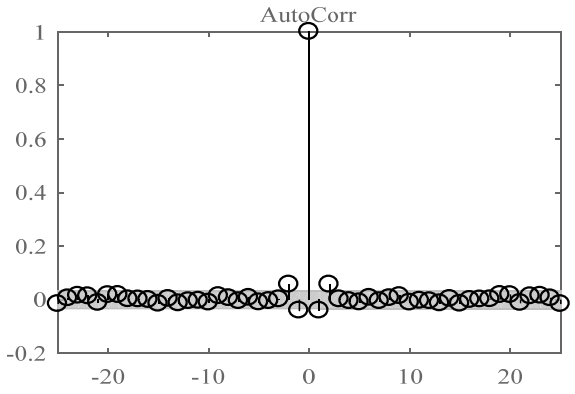

(a)

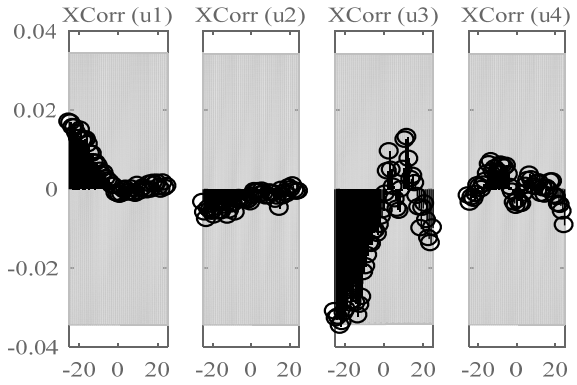

(b)

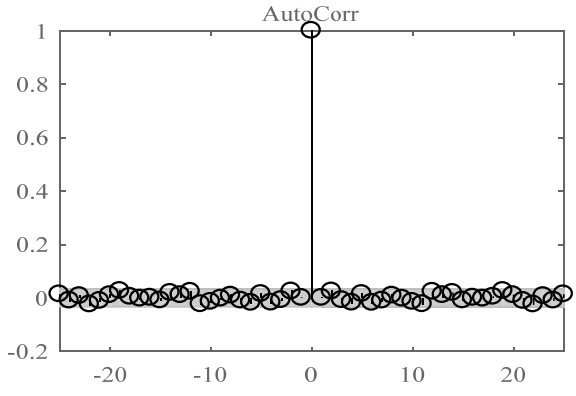

(c)

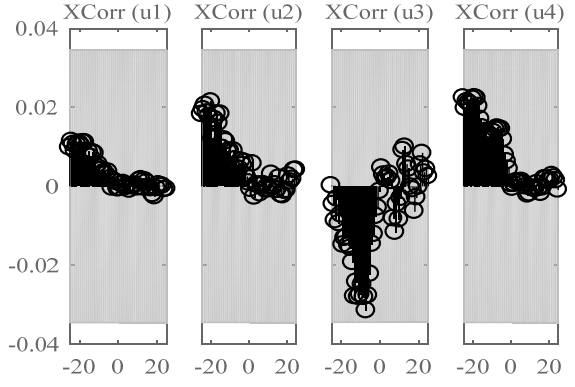

(d)

Figure 23 Experimental identification data for (a) winter and (b) summer

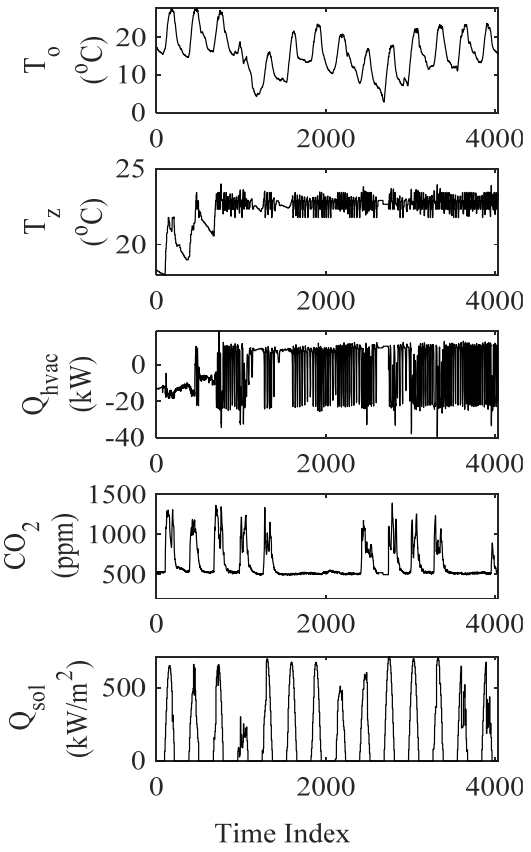

(a)

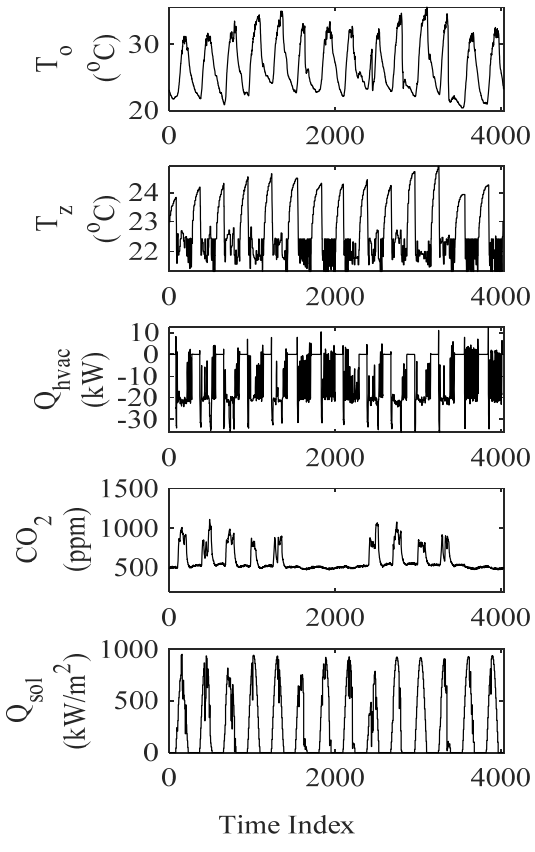

(b)

3.4 Analysis on experimental data (N4SID + PEM)

Figure 23 shows the experimental data. Figure 24 shows the prediction results for the validation datasets. The results for only one day is shown for winter, for clarity. The models predicted the zone temperatures accurately over all the prediction horizons, even though T_a and Q_{sol} were not measured onsite, but were obtained from databases. Figure 25 and Figure 26 show that the models were well trained. Table 3 shows that the identified models using experimental data had better performances that those identified using DesignBuilder data. Although the models for winter had relatively low R^2 values, the TIC values indicate that they had excellent prediction capabilities. Not using the Q_{sol} input had only a minor effect on the resulting model. However, the absence of Q_{sol} in the DesignBuilder input data led to poor models. Similarly, not considering the CO_2 concentration input in the experimental data led to poor models.

Figure 24 Prediction v/s actual temperatures for validation sets of experimental data using N4SID + PEM, (a) one day for winter (b) four days for summer (see online version for colours)

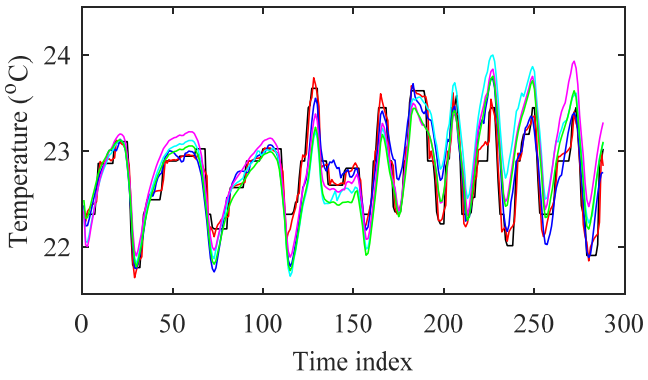

(a)

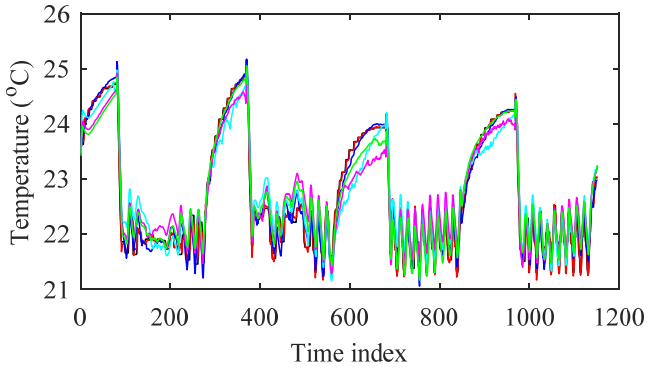

(b)

Each model for the DesignBuilder and experimental data was identified in no time (< 2 s). Getting a suitable grey-box RC model for the optimisation and PEM method took a significant amount of time and expertise to be developed and identified in this work. If experiments were needed to generate persistently exciting data, and if the inputs were obtained through complex processing of measured quantities, the whole process would take even longer. For instance, Viot et al. (2018a) did a significant study to obtain the best RC model for a practical room and the validation MAE was only 0.7°C. In the proposed N4SID + PEM model, the CO_2 concentration was useful as an input, while this approach would not work for an RC model, which is seriously affected by unmeasured disturbances. Thus, alongside the indoor CO_2 level control, the CO_2 measurements can be also useful for the indoor temperature control.

Figure 25 Autocorrelation of residuals for N4SID + PEM, (a) winter (b) summer

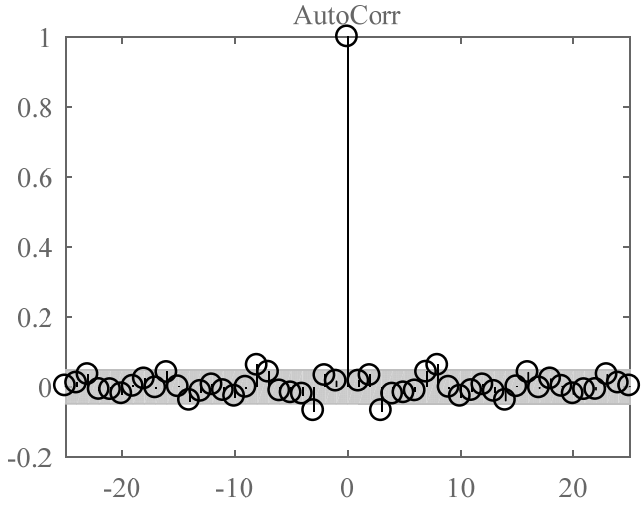

(a)

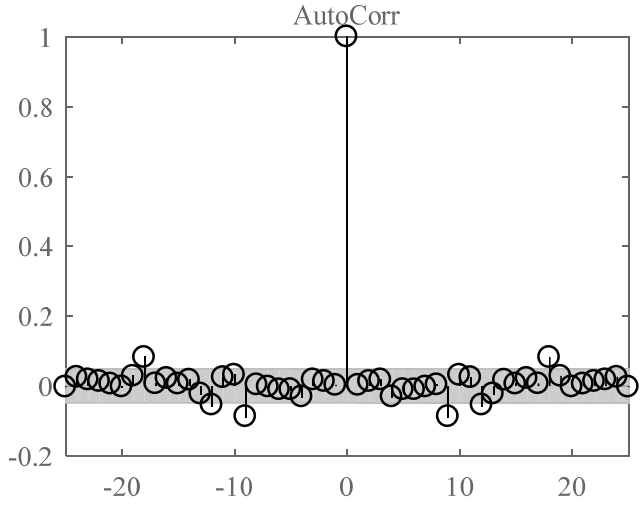

(b)

To further prove the effectiveness of the proposed technique, the model estimated using winter data showed a good performance when validated on the summer data. Similarly, the model estimated using summer data had a good performance when validated using winter data. The detailed results are not shown here due to space limitations.

Table 2 Results of performance evaluation of N4SID + PEM identification for DesignBuilder data

Dataset	*Training*				*Validation*				
Performance indicator	*PAE*	*RMSE*	*MAE*	R^2	*PAE*	*RMSE*	*MAE*	R^2	*TIC*
December – all inputs known	1.44	0.55	0.45	0.94	1.51	0.63	0.52	0.92	0.13
December – occupancy and equipment unknown	1.44	0.55	0.45	0.94	1.51	0.63	0.52	0.92	0.13
July – all inputs known	1.39	0.54	0.44	0.90	1.48	0.64	0.54	0.79	0.21
July – occupancy and equipment unknown	1.39	0.54	0.44	0.90	1.48	0.64	0.54	0.79	0.21
December – noisy – all inputs known	1.57	0.50	0.40	0.95	1.23	0.47	0.39	0.95	0.10
December – noisy – occ. and equipment unknown	1.54	0.50	0.40	0.95	1.22	0.47	0.38	0.95	0.10
July – noisy – all inputs known	1.45	0.54	0.43	0.90	1.33	0.61	0.50	0.81	0.21
July – clean – occ. and equipment unknown	1.45	0.54	0.43	0.90	1.34	0.61	0.50	0.81	0.21

Table 3 Results of performance evaluation of N4SID + PEM identification for experimental data

Dataset	*Training*				*Validation*				
Performance indicator	*PAE*	*RMSE*	*MAE*	R^2	*PAE*	*RMSE*	*MAE*	R^2	*TIC*
Winter – all 4 inputs used	1.20	0.29	0.22	0.95	0.96	0.32	0.26	0.51	0.0070
Winter – GHI unused	1.24	0.33	0.25	0.93	0.87	0.30	0.24	0.57	0.0065
Summer – all 4 inputs used	1.17	0.39	0.31	0.83	0.96	0.26	0.21	0.94	0.0057
Summer – GHI unused	1.25	0.42	0.34	0.80	1.04	0.30	0.24	0.92	0.0066

Figure 26 Cross-correlation of residuals for N4SID + PEM, (a) winter (b) summer

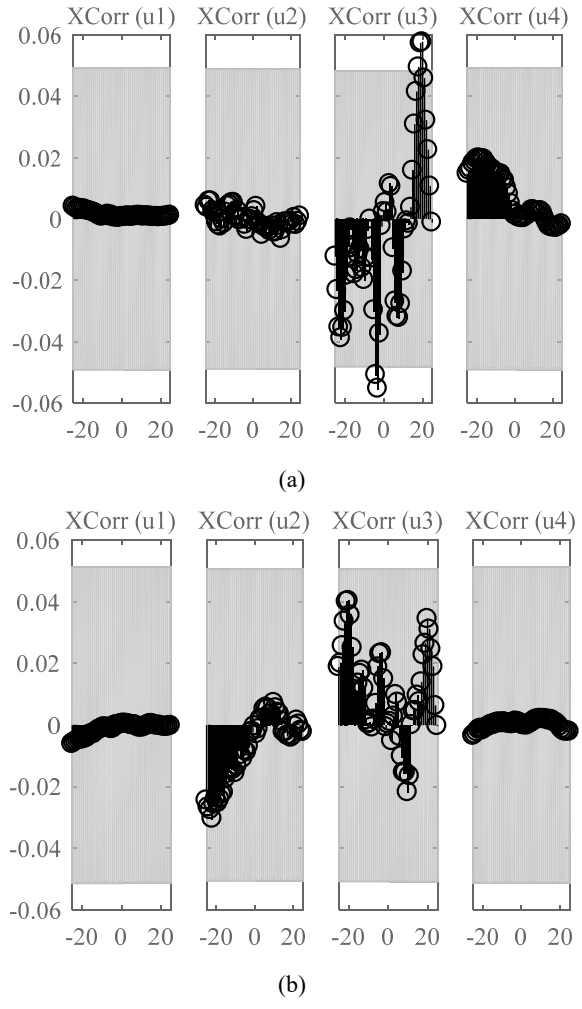

(a)

(b)

4 Conclusions

This paper has shown that an accurate control-oriented LTI model for MPC can be easily and quickly obtained through subspace identification followed by PEM. The models estimated in this work had a good validation performance even if little identification data was used, even in the presence of large unmeasured disturbances and noisy identification data, even if significant nonlinear solar heat gains were present, and even though the identification data was collected during the regular HVAC operation. For the simulation data, the maximum validation PAE, RMSE and MAE were only 1.5°C, 0.64°C and 0.54°C, respectively. For the experimental data, the maximum validation PAE, RMSE and MAE were only 0.96°C, 0.32°C and 0.26°C, respectively. Moreover, the Thiel's inequality coefficients indicated acceptable prediction performances of all the developed models for both simulation and experimental data. The issues associated with the optimisation and PEM techniques for the identification of RC grey-box models were pointed out through analyses using both open-loop and closed-loop data. Particularly, the choice of the objective function, the unknown initial states, the unknown disturbances, the size of the parameter search space and noise in the identification data were found to affect the physical meaning of the identified R and C parameters. It was additionally found that the development and identification of RC grey-box models through the two techniques was very time consuming, even for a single-zone building. The N4SID + PEM technique proposed in this paper could estimate the model for a single-zone building over less than two seconds, and can be considered to be robust, given that the prediction results from a simulated building with a certain type of

construction and operation and located in one climate zone as well as the experimental results from another building with a different type of construction and operation and located in a different climate zone were all satisfactory, for both summer and winter. Further research will apply the proposed method to a multi-zone building. The impacts of the data quality and the pre-processing of data on the identification results will be investigated. Eventually, the developed models will be applied in MPC for a multi-zone building, and the results compared to the baseline HVAC controller.

Acknowledgements

This research did not receive any specific grant from funding agencies in the public, commercial, or not-for-profit sectors. The authors are thankful to Austin R. Coffman and Prabir Barooah from the University of Florida for the experimental data used for analysis in this work.

References

Afram, A. and Janabi-Sharifi, F. (2014) 'Review of modeling methods for HVAC systems', *Applied Thermal Engineering*, Vol. 67, Nos. 1–2, pp.507–519, DOI: 10.1016/j.applthermaleng.2014.03.055.

Arroyo, J., Spiessens, F. and Helsen, L. (2020) 'Identification of multi-zone grey-box building models for use in model predictive control', *Journal of Building Performance Simulation*, Vol. 13, No. 4, pp.472–486, Taylor and Francis Ltd., DOI: 10.1080/19401493.2020.1770861.

Atam, E. and Helsen, L. (2016) 'Control-oriented thermal modeling of multizone buildings: methods and issues: intelligent control of a building system', *IEEE Control Systems*, Vol. 36, No. 3, pp.86–111, DOI: 10.1109/MCS.2016.2535913.

Bäumelt, T. and Dostál, J. (2020) 'Distributed agent-based building grey-box model identification', *Control Engineering Practice*, April, Vol. 101, p.104427, Elsevier Ltd., DOI: 10.1016/j.conengprac.2020.104427.

Blum, D.H. et al. (2019) 'Practical factors of envelope model setup and their effects on the performance of model predictive control for building heating, ventilating, and air conditioning systems', *Applied Energy*, August 2018, Vol. 236, pp.410–425, Elsevier, DOI: 10.1016/j.apenergy.2018.11.093.

Bnhamdoon, O.A.A., Mohamad Hanif, N.H.H. and Akmeliawati, R. (2020) 'Identification of a quadcopter autopilot system via Box-Jenkins structure', *International Journal of Dynamics and Control*, Vol. 8, No. 3, pp.835–850, Springer, Berlin, Heidelberg, DOI: 10.1007/s40435-019-00605-x.

Brastein, O.M. et al. (2018) 'Parameter estimation for grey-box models of building thermal behaviour', *Energy and Buildings*. Vol. 169, pp.58–68, Elsevier B.V., DOI: 10.1016/j.enbuild.2018.03.057.

Cigler, J. and Prívara, S. (2010) 'Subspace identification and model predictive control for buildings', *11th International Conference on Control, Automation, Robotics and Vision, ICARCV 2010*, December, pp.750–755, DOI: 10.1109/ICARCV.2010.5707821.

Coffman, A.R. and Barooah, P. (2017) 'Simultaneous identification of dynamic model and occupant-induced disturbance for commercial buildings', *Building and Environment*, Elsevier Ltd., DOI: 10.1016/j.buildenv.2017.10.020.

Cui, B. et al. (2019) 'A hybrid building thermal modeling approach for predicting temperatures in typical, detached, two-story houses', *Applied Energy*, June 2018, Vol. 236, pp.101–116, DOI: 10.1016/j.apenergy.2018.11.077.

Dadiala, V., Patel, J. and Barve, J. (2020) 'Model predictive control for an industrial coal pulveriser', *International Journal of Modelling, Identification and Control*, Vol. 36, No. 4, pp.353–362, Inderscience Publishers, DOI: 10.1504/IJMIC.2020.117491.

Delcroix, B. et al. (2020) 'Autoregressive neural networks with exogenous variables for indoor temperature prediction in buildings', *Building Simulation*, DOI: 10.1007/s12273-019-0597-2.

Fang, T. and Lahdelma, R. (2016) 'Evaluation of a multiple linear regression model and SARIMA model in forecasting heat demand for district heating system', *Applied Energy*, Vol. 179, pp.544–552, Elsevier Ltd., DOI: 10.1016/j.apenergy.2016.06.133.

Ferracuti, F. et al. (2017) 'Data-driven models for short-term thermal behaviour prediction in real buildings', *Applied Energy*, Vol. 204, pp.1375–1387, Elsevier Ltd., DOI: 10.1016/j.apenergy.2017.05.015.

Guo, M., Gu, D. and Su, Y. (2017) 'System identification of the quadrotor with inner loop stabilisation system', *International Journal of Modelling, Identification and Control*, Vol. 28, No. 3, p.245, DOI: 10.1504/ijmic.2017.10007049.

Hu, M. et al. (2019) 'Price-responsive model predictive control of floor heating systems for demand response using building thermal mass', *Applied Thermal Engineering*, Elsevier Ltd., DOI: 10.1016/j.applthermaleng.2019.02.107.

IEA (2019) *IEA the Critical Role of Buildings* [online] https://www.iea.org/reports/the-critical-role-of-buildings (accessed 5 April 2020).

Joe, J. and Karava, P. (2017) 'Agent-based system identification for control-oriented building models', *Journal of Building Performance Simulation*, Vol. 10, No. 2, pp.183–204, Taylor and Francis Ltd., DOI: 10.1080/19401493.2016.1212272.

Kim, D. et al. (2020) 'A methodology for generating reduced-order models for large-scale buildings using the Krylov subspace method', *Journal of Building Performance Simulation*, Vol. 13, No. 4, pp.419–429, Taylor and Francis Ltd., DOI: 10.1080/19401493.2020.1752309.

Kim, W. and Katipamula, S. (2018) 'A review of fault detection and diagnostics methods for building systems', *Science and Technology for the Built Environment*, Vol. 24, No. 1, pp.3–21, Taylor and Francis Inc., DOI: 10.1080/23744731.2017.1318008.

Li, J. et al. (2010) 'Dynamic zone modelling for HVAC system control', *International Journal of Modelling, Identification and Control*, Vol. 9, Nos. 1–2, pp.5–14, Inderscience Publishers, DOI: 10.1504/IJMIC.2010.032354.

Martincevic, A. and Vasak, M. (2019) 'Constrained Kalman filter for identification of semiphysical building thermal models', *IEEE Transactions on Control Systems Technology*, IEEE, pp.1–8, DOI: 10.1109/tcst.2019.2942808.

MathWorks (2021) *What is Residual Analysis? – MATLAB & Simulink*, MathWorks Italia [online] https://it.mathworks.com/help/ident/ug/what-is-residual-analysis.html (accessed 7 April 2021).

Privara, S. et al. (2012) 'Incorporation of system steady state properties into subspace identification algorithm', *International Journal of Modelling, Identification and Control*, Vol. 16, No. 2, pp.159–167, Inderscience Publishers, DOI: 10.1504/IJMIC.2012.047123.

Prívara, S. et al. (2013) 'Building modeling as a crucial part for building predictive control', *Energy and Buildings*, Vol. 56, pp.8–22, DOI: 10.1016/j.enbuild.2012.10.024.

Radecki, P. and Hencey, B. (2017) 'Online model estimation for predictive thermal control of buildings', *IEEE Transactions on Control Systems Technology*, Vol. 25, No. 4, pp.1414–1422, DOI: 10.1109/TCST.2016.2587737.

Ryzhov, A. et al. (2019) 'Model predictive control of indoor microclimate: existing building stock comfort improvement', *Energy Conversion and Management*, October 2018, Vol. 179, pp.219–228, Elsevier, DOI: 10.1016/j.enconman.2018.10.046.

Salakij, S. et al. (2016) 'Model-based predictive control for building energy management. I: energy modeling and optimal control', *Energy and Buildings*, Vol. 133, pp.345–358, DOI: 10.1016/j.enbuild.2016.09.044.

Salem, F.M., Mosaad, M.I. and Awadallah, M.A. (2015) 'A comparative study of MPC and optimised PID control', *International Journal of Industrial Electronics and Drives*, Vol. 2, No. 4, p.242, Inderscience Publishers, DOI: 10.1504/ijied.2015.076293.

Schubnel, B. et al. (2020) 'State-space models for building control: how deep should you go?', *Journal of Building Performance Simulation*, Vol. 13, No. 6, pp.707–719, DOI: 10.1080/19401493.2020.1817149.

Tang, R. and Wang, S. (2019) 'Model predictive control for thermal energy storage and thermal comfort optimization of building demand response in smart grids', *Applied Energy*, February, Vol. 242, pp.873–882, Elsevier, DOI: 10.1016/j.apenergy.2019.03.038.

Ürge-Vorsatz, D. et al. (2015) 'Heating and cooling energy trends and drivers in buildings', *Renewable and Sustainable Energy Reviews*, pp.85–98, Elsevier Ltd., DOI: 10.1016/j.rser.2014.08.039.

Viot, H. et al. (2018a) 'Model predictive control of a thermally activated building system to improve energy management of an experimental building: Part I – modeling and measurements', *Energy and Buildings*, Vol. 172, pp.94–103, Elsevier B.V., DOI: 10.1016/j.enbuild.2018.04.055.

Viot, H. et al. (2018b) 'Model predictive control of a thermally activated building system to improve energy management of an experimental building: Part II – potential of predictive strategy', *Energy and Buildings*, Vol. 172, pp.385–396, Elsevier B.V., DOI: 10.1016/j.enbuild.2018.04.062.

Wang, J., Chen, H. et al. (2019a) 'A novel efficient optimization algorithm for parameter estimation of building thermal dynamic models', *Building and Environment*, Elsevier Ltd., DOI: 10.1016/j.buildenv.2019.02.006.

Wang, J., Li, S. et al. (2019b) 'Data-driven model predictive control for building climate control: three case studies on different buildings', *Building and Environment*, March, Vol. 160, p.106204, Elsevier, DOI: 10.1016/j.buildenv.2019.106204.

Wang, Z. and Chen, Y. (2019) 'Data-driven modeling of building thermal dynamics: methodology and state of the art', *Energy and Buildings*, Vol. 203, Elsevier B.V., DOI: 10.1016/j.enbuild.2019.109405.

Nomenclature

List of symbols	
Abbreviations	
ARX	Autoregressive model with exogenous inputs
GHI	Global horizontal irradiance
HVAC	Heating, ventilation and air-conditioning
IPG	Initial parameter vector guess
LTI	Linear time invariant
MAE	Mean absolute error
MAPE	Mean absolute percentage error
MPC	Model predictive control
NR	Narrow range
PAE	Peak absolute error
PEM	Prediction-error-minimisation
RC	Resistance-capacitance
RMSE	Root mean square error
SAE	Sum of absolute error
SSE	Sum of squared error
TIC	Theil's inequality coefficient
WR	Wide range
Symbols	
A	Solar convective heat transfer factor [m^2]
B	Solar radiative heat transfer factor [m^2]
C	Solar factor affecting envelope [m^2]
Cx	Thermal capacitance [kJ/K]
D	Radiative proportion of disturbance
Q	Heat flow [kW]
R	Thermal resistance [K/kW]
T	Temperature [°C]
U	Heat transfer coefficient [$W/m^2.K$]
α	Exterior proportion of envelope thermal resistance
Subscripts	
dist	Disturbance
e	Envelope
g	Glazing
im	Internal mass
o	Outside air
sol	Solar
z	Zone air